

Investigating Self-Assembled Protein Nanotubes Using Atomic Force Microscopy

Lijiang NIU BSc. MSc.

**Thesis submitted to the University of Nottingham
for the degree of Doctor of Philosophy**

July 2009

温故而知新

By reviewing the old, gain the knowledge of the new.

孔子

Confucius

Abstract

Self-assembled protein nanotubular materials are attractive as putative building blocks for a variety of applications. Knowledge of the three-dimensional structures and the physical properties of these protein nanotubes then becomes a prerequisite for their use in rational materials design. The main purpose of the work presented in this thesis is to investigate both the structural and mechanical properties of protein nanotubes utilizing atomic force microscopy (AFM). Several different protein nanotubes will be used as exemplars to develop AFM methods.

AFM is capable of both visualizing and monitoring dynamic processes. Within this thesis, not only could the change in morphology of protein nanotubes be visualized by AFM, but also changes in their mechanical properties were monitored as dynamic processes. For example, changes in the morphology (in chapter 3) and flexibility (in chapter 4) of lysozyme fibrils during fibrillization were investigated.

Chapters 4 to 6 describe a range of different methods to obtain the mechanical properties of protein nanotubes: the persistence length method (chapter 4), the adhesive interaction method (chapter 5) and the bending beam method (chapter 6). All of these had their own advantages. However, each method was found only to be suitable for protein nanotubes with elasticities within a defined range.

The protein nanotubes investigated by AFM in the thesis included *Salmonella* flagellar filaments, lysozyme fibrils and diphenylalanine (FF) nanotubes. All of the investigated protein nanotube structures had Young's moduli lying between

that of gelatin and bone. This highlights their potential, in terms of mechanical properties, for a range of applications in drug-delivery systems and tissue-engineering scaffolds. In future, if a database of mechanical properties of protein nanotubes could be built up using the AFM methods developed and utilized within this thesis, the development of the applications of protein nanotubes will be accelerated, as the right protein nanotubes will be selected for appropriate applications.

Acknowledgements

I would like to thank my supervisors, Professor Saul J. B. Tendler and Dr. Stephanie Allen, for their guidance and various contributions towards this thesis and their constant support.

I would like to thank all my colleagues within the LBSA group for their support and a lot of useful discussions. Many thanks to Dr Xinyong Chen for his help with lots of AFM technical issues and to Dr. Alberto Orta for developing software Veca for data analysis in this thesis.

I wish to thank Dr. Richard Woods (Genetics group, Queen's Medical Centre) for kindly providing *Salmonellar* flagellar filament samples and showing me the sample preparation process. I also thank Dr. Claudio Canale (Università degli Studi di Genova, Italy) for kindly providing β 2-microglobulin protein samples.

I would like to thank all the lovely friends I have made in Nottingham. I thank my parents for always being supportive and forgiving to me. Last but not least I thank my husband and my daughter for being in my life.

List of Contents

Abstract	i
Acknowledgements	iii
List of Contents	iv
List of Tables	ix
List of Figures	x
Chapter 1 Introduction: Protein Nanotubes Are Novel Bio-inspired Materials ..	1
1.1 Protein Nanotubes	1
1.2 Bacterial Flagellar Filaments	4
1.2.1 Bacterial Flagellum	4
1.2.1.1 Motor Function	4
1.2.1.2 Overall Structure	5
1.2.1.3 Self-assembly Process	5
1.2.2 The Bacterial Flagellar Filament	8
1.2.2.1 Bacterial Flagellin	10
1.2.2.2 Intersubunit Interactions in the Filament	11
1.2.2.3 Transformations of Flagellar Filaments in vitro	15
1.2.3 Applications of Bacterial Flagellar Filaments	17
1.3 Amyloid Fibrils	20
1.3.1 Protein Misfolding	20
1.3.1.1 Protein Misfolding and Diseases	20
1.3.1.2 Energy Landscape of Protein Folding	22

1.3.1.3 Structure of Amyloid Fibrils	24
1.3.2 Applications of Amyloid Fibrils	29
1.3.3 Diphenylalanine Nanotubes (FF Nanotubes)	33
1.3.3.1 Discovery and Synthesis of Diphenylalanine Nanotubes	33
1.3.3.2 Structures and Properties of diphenylalanine Nanotubes.....	35
1.3.3.3 Applications of Diphenylalanine Nanotubes	39
1.4 Aims and Outline of Research	42
Chapter 2 Instrumental and Experimental Methods	44
2.1 Atomic Force Microscopy	44
2.1.1 Atomic Force Microscopy.....	44
2.1.1.1 Principle of AFM	45
2.1.1.2 Operation Modes of AFM.....	47
2.1.1.3 Force Measurements by AFM.....	48
Conversion of force curves	49
Problem of zero tip-sample distance	50
Determination of spring constant of the cantilever	52
2.1.2 AFM Analysis	54
AFM Imaging.....	54
AFM force measurements	55
2.1.3 Image Processing	55
2.2 Preparation of Protein Nanotubes	56
2.2.1 Bacterial Flagellar Filaments	56
2.2.2 Lysozyme Fibrils.....	57
2.2.3 β 2-Microglobulin Fibrils.....	57

2.2.4 Diphenylalanine Nanotubes (FF Nanotubes)	57
2.2.5 Sample Preparation for AFM Analysis	58
Substrates employed for AFM analysis	58
General sample preparation protocols for AFM analysis	60
Chapter 3 Dynamic Processes of Assembly and Degradation of Protein	
Nanotubes	62
3.1 Flagellar Filaments in Different Environment	62
3.1.1 Flagellar Filaments on Mica in Air	62
3.1.2 Dissociation of Flagellar Filaments in Low pH Environment	64
3.1.2.1 Salmonella Flagellar Filaments in Neutral Condition.....	65
3.1.2.2 Salmonella Flagellar Filaments in Weak Acidic Condition.....	66
3.1.2.3 Salmonella Flagellar Filaments in Alkaline Condition.....	67
3.1.2.4 Dissociation of Salmonella Flagellar Filaments in Acidic Condition	
.....	70
3.1.2.5 Direct Observation of the Dissociation of Salmonella Flagellar	
Filaments in Acidic Condition	72
3.1.3 Flagellar Filaments on Gold Surface.....	73
3.1.3.1 <i>Salmonella</i> Flagellar Filaments imaged in Air on Gold Surfaces.	73
3.1.3.2 The <i>Salmonella</i> Flagellar Filaments in Propanol on Gold Surface	74
3.2 Fibrillization Processes of Lysozyme	76
3.2.1 Preparation of Lysozyme Samples.....	77
3.2.2 The Early Stages of Lysozyme Fibrillization.....	80
3.2.3 The Middle Stages of Fibrillization	82
3.2.4 The Late Stages of Lysozyme Fibrillization	88

3.3 Alternative Assembly of Tubular and Spherical Nanostructures from FF Peptides	90
3.4 Conclusion	95
Chapter 4 Persistence Length Study of Protein Nanotubes	96
4.1 Theory and Method	96
4.1.1 Persistence Length is a Measure of the Flexibility of a Filament	96
4.1.2 Analysing AFM Images of Nanofibrils and Nanotubes to Obtain Their Persistence Lengths	98
4.2 The Persistence Length of Flagellar Filaments in Different Environments	103
4.3 Change of Flexibility during Fibrillization of Lysozyme Fibrils	108
4.4 Flexibility of diphenylalanine Fibrils	111
4.5 Conclusion	113
Chapter 5 Using the Adhesive Interaction between AFM Tips and Sample Surfaces to Measure the Elasticity of Protein Nanotubes	115
5.1 Theory and Method	115
5.1.1 The JKR (Johnson, Kendall and Roberts) Model	115
5.1.2 Applying JKR Model to Obtain the Young's Modulus of a Sample ..	121
5.2 The Effects of the Ionic Strength on the Elasticity of <i>Salmonella</i> Flagellar Filaments	125
5.3 Investigating the Interaction between <i>Salmonella</i> Flagellar Filaments and Mica Substrates in Electrolyte Environments	129
5.4 Conclusion	133

Chapter 6 Using the Bending Beam Model to Estimate the Elasticity of Protein Nanotubes	134
6.1 Theory	134
6.1.1 Deformation of a Fixed-End Bending Beam	134
6.1.2 Applying the Bending Beam Model to Nanotubes	135
6.2 β 2-microglobulin Fibrils Lying over Gaps within the Gold Substrate	137
6.3 Elasticity of diphenylalanine Fibrils	139
6.3.1 Elasticity of FF Nanotubes at Room Temperature.....	140
What is a “good” deflection?	140
Is the deflection reversible?	142
Obtaining E and G.....	143
Determination of D effects the resulting E and G.....	145
6.3.2 Effect of Temperature on the Elasticity of FF	146
6.3.3 Effect of Humidity on the Elasticity of FF Nanotubes	149
6.4 Conclusion	151
Chapter 7 Final Conclusions: AFM is a Powerful Tool for Investigating the Properties of Protein Nanotubes	153
7.1 AFM Methods of Investigating Protein Nanotubes	153
7.2 The Mechanical Properties of Protein Nanotubes.....	155
7.3 Future Directions.....	156
References	158
Publication	174

List of Tables

Table 1-1 Examples of amyloidogenic peptides and proteins.....	21
Table 3-1 The dimensions of <i>Salmonella</i> flagellar filaments observed in AFM images obtained in liquid.	69
Table 3-2 The average height of <i>Salmonella</i> flagellar filaments on gold surface in a series of propanol-water mixtures.	75
Table 3-3 The average heights of 6 types of lysozyme fibrils observed.	83
Table 3-4 The predicated heights using Khurana’s model (2003).	84
Table 3-5 The predicated heights using the “n+1” model.	85
Table 3-6 The summary of the experimental data of the heights of lysozyme fibrils and the heights predicted by Khurana’s model and “n+1” model.	86
Table 4-1 <i>Salmonella</i> flagellar filaments in different environments.....	106
Table 4-2 Persistence length of lysozyme protofilaments and fibrils of different assembly levels during fibrillization.	108
Table 5-1 Young’s modulus E of <i>Salmonella</i> flagellar filaments in buffer solutions with different concentrations of Mg^{2+}	125
Table 5-2 Young’s modulus E of <i>Salmonella</i> flagellar filaments in buffer solutions with different ionic strength.	126
Table 5-3 Summary of Young’s modulus E of <i>Salmonella</i> flagellar filaments in different buffer solutions.....	126
Table 6-1 The reversible indentation of a FF nanotube over a hole under the loading force of AFM tip.	142

List of Figures

Figure 1-1 Ghadiri <i>et al.</i> protein nanotubes.	2
Figure 1-2 Electron micrograph of a negatively-stained bacterium, <i>Salmonella typhimurium</i>	4
Figure 1-3 Schematic diagrams showing the overall architecture of the bacterial flagellum..	6
Figure 1-4 Outward assembly pathway of the flagellum..	9
Figure 1-5 The C α backbone trace, hydrophobic side-chain distribution and structural information of flagellin..	11
Figure 1-6 Polymorphic model of the filament.....	12
Figure 1-7 The surface lattice of L- and R-type straight flagellar filaments.....	13
Figure 1-8 Three-dimensional density map of the flagellar filament (R-type straight filament), calculated by including data up to 9 Å..	14
Figure 1-9 Ribbon diagram of the C α backbone of the filament model in stereo view.....	15
Figure 1-10 Dark field light micrographs of <i>Salmonella</i> flagellar filaments.....	17
Figure 1-11 TEM images of disulfide cross-linked Cys-loop flagella bundles stained with 2% phosphotungstic acid (pH7.5).....	19
Figure 1-12 TEM images of gold nanoparticles that were synthesized by reduction of Au(I) on a histidine loop peptide flagella scaffold	19
Figure 1-13 Stereo ribbon diagram of the structure of (a) lysozyme (b) beta2-microglobulin	22

Figure 1-14 The estimated energy landscape diagram based on data for the folding of lysozyme..	23
Figure 1-15 A molecular model of an amyloid fibril grown from an SH3 domain.	25
Figure 1-16 Khurana's model for the hierarchical assembly of insulin into amyloid fibrils..	26
Figure 1-17 A general scheme of the multipathway fibrilization of insulin.	27
Figure 1-18 AFM height images of insulin amyloid.....	28
Figure 1-19 AFM images of 0.1% (w/w) insulin, aggregated at 60 °C for six days in: (a) water; (b) 5% (w/w) EtOH; (c) 20% (w/w) EtOH; (d) 40% (w/w) EtOH .	29
Figure 1-20 Gold and silver enhancement of NM fibres..	31
Figure 1-21 Electrical behavior of NM-templated metallic fibres.....	32
Figure 1-22 (a) Schematic structure of FF. (b) The molecular structure of FF from the single crystal structure determination..	34
Figure 1-23 Model for the construction of hollow FF fibres..	36
Figure 1-24 SEM images of controlled patterning of aligned diphenylalanine nanotubes.	38
Figure 1-25 AFM topography images of aligned FF nanotubes.....	38
Figure 1-26 Casting of silver nanowires with the peptide nanotubes.	39
Figure 1-27 SEM images of (a) peptide nanotubes and nanovesicles containing Pt particles (inset: tilted image showing the tubes are hollow) and (b) a high resolution TEM image showing the 2 nm Pt nanoparticles embedded in the wall of a platinum nanotube.	40
Figure 1-28 Integrating FF nanotubes in micro-fabrication processes..	41

Figure 2-1 Schematic of the concept of AFM and the optical lever.	46
Figure 2-2 Photos of a general purpose silicon nitride cantilever produced by Veeco Probes.....	46
Figure 2-3 A model force measurement curve recorded for an infinitely hard material surface with no surface forces.....	50
Figure 2-4 A force measurement retracting curve for a deformable material with attraction and adhesion forces.....	51
Figure 2-5 Measurement of the dimensions of a protein nanotube from an AFM height image using SPIP.	56
Figure 2-6 AFM height image of gold substrate obtained using evaporation gold coater.....	59
Figure 2-7 An AFM height image of a micropatterned silicon substrate with holes of $5\ \mu\text{m} \times 5\ \mu\text{m}$ and 200 nm in depth.	59
Figure 3-1 Tapping mode AFM height images of <i>Salmonella</i> flagellar filaments in air on mica.....	63
Figure 3-2 Histogram of the contour length measured for <i>Salmonella</i> flagellar filaments on mica in air.....	64
Figure 3-3 A sketch demonstrates that Mg^{2+} works as a bridge between flagellar filaments and the mica surface in pH 7.0 buffer solution.	64
Figure 3-4 A height image of <i>Salmonella</i> flagellar filaments taken in pH 7.0 buffer solution (10 mM PBS & 10 mM MgCl_2) using tapping mode AFM.	66
Figure 3-5 A height image of <i>Salmonella</i> flagellar filaments taken in HCl solution (pH 4.4) using tapping mode AFM.	67

Figure 3-6 A height image of <i>Salmonella</i> flagellar filaments taken in pH 10.0 solution (0.1mM NaOH & 10 mM MgCl ₂) using tapping mode of AFM.	68
Figure 3-7 Sketch of an example of "tip broadening" effect on a filament.	69
Figure 3-8 A height image of <i>Salmonella</i> flagellar filaments taken in pH 4.0 solution using tapping mode of AFM.	71
Figure 3-9 Height images of <i>Salmonella</i> flagellar filaments in liquid using tapping mode AFM.	72
Figure 3-10 Tapping mode AFM height images of <i>Salmonella</i> flagellar filaments in air on gold.	74
Figure 3-11 Tapping mode AFM height images of <i>Salmonella</i> flagellar filaments in 80% propanol on gold.	75
Figure 3-12 A plot of average height of <i>Salmonella</i> flagellar filaments vs. percentage of propanol in propanol-water buffer.	76
Figure 3-13 An AFM height image of 10 mM glycine buffer obtained using tapping mode AFM before (a) and after (b) incubation at 57 ± 2 °C for 2 weeks.	78
Figure 3-14 An AFM height image in tapping mode of 10mg/mL lysozyme in 10mM glycine buffer at pH 2.0.	79
Figure 3-15 Histogram of the height of lysozyme particles before incubation measured from AFM images taken on mica in air.	79
Figure 3-16 An AFM height image of lysozyme after 3 days of incubation.	80
Figure 3-17 AFM image of one lysozyme fibril with clear periodicity after 2 days of incubation.	81
Figure 3-18 AFM height image of lysozyme fibrils after 4 days of incubation...	82

Figure 3-19 A model for the hierarchical assembly of insulin into amyloid fibrils..	84
Figure 3-20 “n+1” model for lysozyme fibrils assembly.	85
Figure 3-21 An AFM height image of a lysozyme fibril after 4 days of incubation.	87
Figure 3-22 An AFM height image of lysozyme fibrils after 11 days of incubation.....	88
Figure 3-23 AFM height images of lysozyme fibrils after 14 days of incubation.	89
Figure 3-24 AFM image of typical long and thick FF nanotubes along with short and thin fibrillar structures.	91
Figure 3-25 SEM images of (a) peptide nanotubes and (b) a mixture of nanotubes and vesicles	92
Figure 3-26 An AFM image of FF nanostructures self-assembled at 40°C.....	94
Figure 3-27 An AFM image of FF nanostructures self-assembled at 65°C.....	94
Figure 4-1 A sketch of a thin flexible filament.	97
Figure 4-2 An AFM tapping mode height image of <i>Salmonella</i> flagellar filaments observed on mica in air.	99
Figure 4-3 Use of “Freehand” tool to trace the contour of a filament within Veca.	99
Figure 4-4 The contour of the filament shown in Figure 4-2 is digitalised to XY-coordinate sets here.	101
Figure 4-5 Persistence length P against contour segment length l	102

Figure 4-6 The plot of the mean square end-to-end distance $\langle R^2 \rangle$ against the contour length s of the filament on Figure 4-2	102
Figure 4-7 Histogram of the persistence length obtained for <i>Salmonella</i> flagellar filaments on mica in air through the application of Equation 4-2	104
Figure 4-8 Tapping mode AFM height image of <i>Salmonella</i> flagellar filaments in air on gold.	105
Figure 4-9 AFM image of FF nanotubes.....	112
Figure 5-1 The adhesive interaction between the AFM tip and the sample.....	116
Figure 5-2 A force-versus-displacement approach curve.	121
Figure 5-3 The force-versus-indentation retract curve from the same experiment of Figure 5-2 . (a) is the whole retract curve and (b) is zoomed part of the curve. Reading from (b), there are $P_{\delta=0} = 0.69$ nN and $\delta_{P=0} = 6.7$ nm.	122
Figure 5-4 Histogram of Young's modulus E of <i>Salmonella</i> flagellar filaments on mica in PBS buffer with $MgCl_2$ ($I = 0.1$ M, $c_{PBS} = 0.01$ M, $c_{Mg^{2+}} = 0.01$ M, pH 7.0) obtained using adhesive interaction method.	124
Figure 5-5 The force-versus-indentation retract curve from the control experiment.....	124
Figure 5-6 Young's modulus E of <i>Salmonella</i> flagellar filaments versus the ionic strength I of buffer solutions.....	127
Figure 5-7 A force-versus-indentation retracting curve of <i>Salmonella</i> flagellar filaments on mica surface in pH 7.0 buffer ($c_{PBS} = 0.01$ M) without Mg^{2+}	130
Figure 5-8 Histogram of desorption forces of <i>Salmonella</i> flagellar filaments from mica surface in pH 7.0 buffer without Mg^{2+}	131

Figure 6-1 Schematic of the suspended beam configuration produced by a protein nanotube lying over a cavity on the substrate.	136
Figure 6-2 AFM height image of β 2-microglobulin fibrils after 5 days of incubation.	138
Figure 6-3 AFM image of β 2-microglobulin fibrils obtained in water on gold surfaces.	138
Figure 6-4 Examples of FF nanotubes lying over holes of the silicon substrate with different deflections.	141
Figure 6-5 AFM images of a single FF nanotube on a silicon grid.	144
Figure 6-6 The graph of $1/E_{\text{bending}}$ against $1/L^2$ of the fibril in Figure 6-5	144
Figure 6-7 AFM images of FF nanotubes at different temperatures.	147
Figure 6-8 AFM images of FF nanotubes at different relative humidities.	150
Figure 7-1 Young's modulus of different materials.	156

Chapter 1 Introduction: Protein Nanotubes Are Novel Bio-inspired Materials

Self-assembled protein nanotubular materials are attractive as potential building blocks for a variety of applications, not only because of their biocompatibility and chemical modifiability, but also because of their large-scale production ability and manufacture through simple experimental procedures in laboratories. Knowledge of the three-dimensional structures and the physical properties of these protein nanotubes then becomes a prerequisite for rational materials design. The main purpose of the work presented in this thesis is to investigate how to obtain the structural and mechanical information of protein nanotubes.

In this chapter, I will firstly review the previous studies on the synthesis, properties and applications of protein nanotubes, with a particular focus on the systems studied in this thesis, namely, bacterial flagellar filaments and amyloid fibrils. I will then outline the aim and the design of the work presented in the subsequent chapters in this thesis.

1.1 Protein Nanotubes

There has been rapid progress in the development of nano-scale materials, such as nanowires, nanotubes and nanoparticles. Carbon nanotubes have attracted a great deal of attention and have been used for a number of nano-scale devices. Some of these devices show significant improvements compared to existing devices (Chen *et al.* 2003; Fennimore *et al.* 2003; Modi *et al.* 2003; Melosh *et al.*

2003; Zhong *et al.* 2003). However, carbon nanotubes have been produced by expensive techniques, including arc discharge (Ebbesen and Ajayan 1992), laser ablation (Guo *et al.* 1995a; 1995b), and chemical vapor deposition (CVD) (Li *et al.* 1996). Most of these processes take place in vacuum or with process gases.

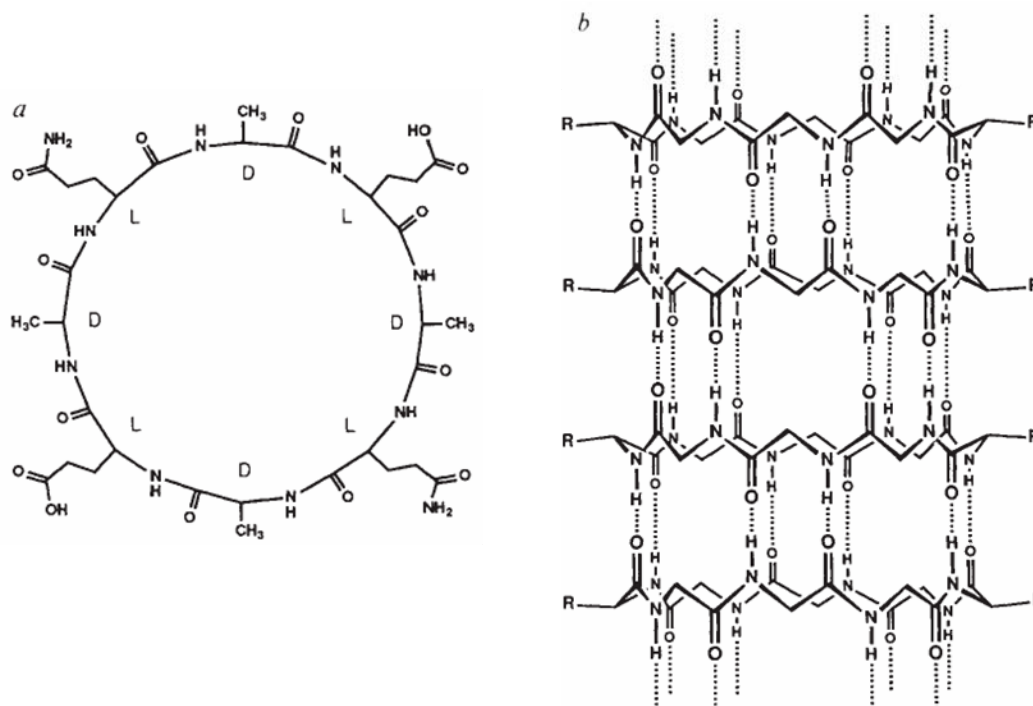


Figure 1-1 Ghadiri *et al.* protein nanotubes. (a) The chemical structure of the peptide subunit. (b) Self-assembled tubular configuration (figure adapted from Ghadiri *et al.* 1993).

Protein nanotubes have structures that possess a well-defined hollow cylinder with a diameter range of 0.5-500nm and an aspect ratio greater than five (Gao 2005). Ghadiri *et al.* brought the definition of protein nanotubes (PNT's) into history by demonstrating that cyclic polypeptides with an even number of alternating D- and L-amino acids can self-assemble into a desired nanotubular structure through intermolecular hydrogen bonding (Figure 1-1) (Ghadiri *et al.*

1993). Since then, protein nanotubes have been employed in order to both explore and control molecular aggregation processes (via non-covalent interactions) and to understand the underlying mechanisms of prion and neurodegenerative diseases (Greig and Philip 2001; Harper and Lansbury 1997; Sipe and Cohen 2000). Recently, studies have also been carried out on how to use protein nanotubes as nano-scale devices. The advantages of this over the use of other materials is that, 1) protein nanotubes can be produced by self-assembly processes in vivo and in vitro under mild conditions, ie. room temperature and atmospheric pressure; 2) protein nanotubes can be produced at a large-scale with relatively small cost; 3) smart functionalities for cross-linking and conjugation to other molecules can be added at desired positions in protein nanotubes through well-established chemical and peptide synthetic methods. However, this field is still in the early stages of development. Most of the reports in the literature are of protein nanotubes synthesis (Zhao *et al.* 2008); though some promising results of their use in applications are beginning to appear. The potential applications of protein nanotubes include for targeted drug-delivery systems, tissue-engineering scaffolds and biosensing devices (Krejцова and Rabiskova 2008; Djalali *et al.* 2003; Zhang 2003; Bong *et al.* 2001; Bong and Ghadiri 2001; Yemini *et al.* 2005a; 2005b). In order to discover more potential applications of protein nanotubes, studies of their morphology and physical properties becomes a prerequisite.

1.2 Bacterial Flagellar Filaments

1.2.1 Bacterial Flagellum

1.2.1.1 Motor Function

Bacteria swim actively in liquid environments. They can sense stimuli such as chemicals (Mesibov and Adler 1972; Seymour and Doersch 1973; Tso and Adler 1974) and temperature (Maeda *et al.* 1976) in their immediate environment and change their swimming patterns to move towards favourable, or away from unfavourable conditions, for their survival. These behaviours are called taxis. The bacterial flagellum is the organelle by means of which bacteria swim (**Figure 1-2**).

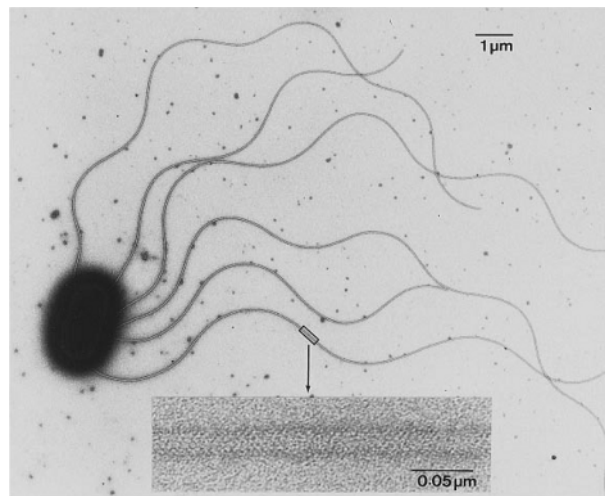


Figure 1-2 Electron micrograph of a negatively-stained bacterium, *Salmonella typhimurium* (figure adapted from Namba and Vonderviszt 1997).

Bacteria swim by rotating their flagellar filaments (Yonekura *et al.* 2002). The fuel for rotation is the membrane gradient of ions, H^+ in most neutrophiles and Na^+ in alkalophiles and marine *Vibrio* species (Hirota *et al.* 1981). The proton-

driven motor rotates at 300 Hz, whereas the sodium-driven motor rotates at up to 1700 Hz (Berry and Armitage 1999; Berg 2002; Oster and Wang 2003). In most species, the motors can rotate either clockwise (CW) or counter clockwise (CCW), and cells direct their movement by regulating switching between the two directions. In *Escherichia coli* or *Salmonella*, for example, CCW rotation allows several filaments on a cell to join in a bundle and drive the cell smoothly forward (a ‘run’), whereas CW rotation disrupts the filament bundle and causes rapid somersaulting (a ‘tumble’) (Blair 2003). This leads to the tactic behaviour, moving towards environments that promote survival (Namba and Vonderviszt 1997; Yonekura *et al.* 2002) at a speed of several body lengths a second (Berry and Armitage 1999).

1.2.1.2 Overall Structure

The flagellum consists of a helical filament connected via the hook to the so-called ‘basal-body’, which is surrounded by a ring of torque-generating particles in the cytoplasmic membrane (**Figure 1-3**). These particles are anchored to the cell wall and are necessary for torque generation. In mechanical terms, the filament is the propeller, and the basal-body and torque-generating particles together are the motor. Within the motor, the basal-body is the ‘rotor’ and rotates (along with the hook and filament) relative to the anchored torque-generating particles or ‘stator’ (Berry and Armitage 1999).

1.2.1.3 Self-assembly Process

The assembly process of the bacterial flagellum starts from the formation of the FliF ring (also called the MS ring, see **Figure 1-3**) complex in the cytoplasmic

membrane, and proceeds in both inward and outward directions, as well as laterally (Figure 1-4) (Namba and Vonderviszt 1997).

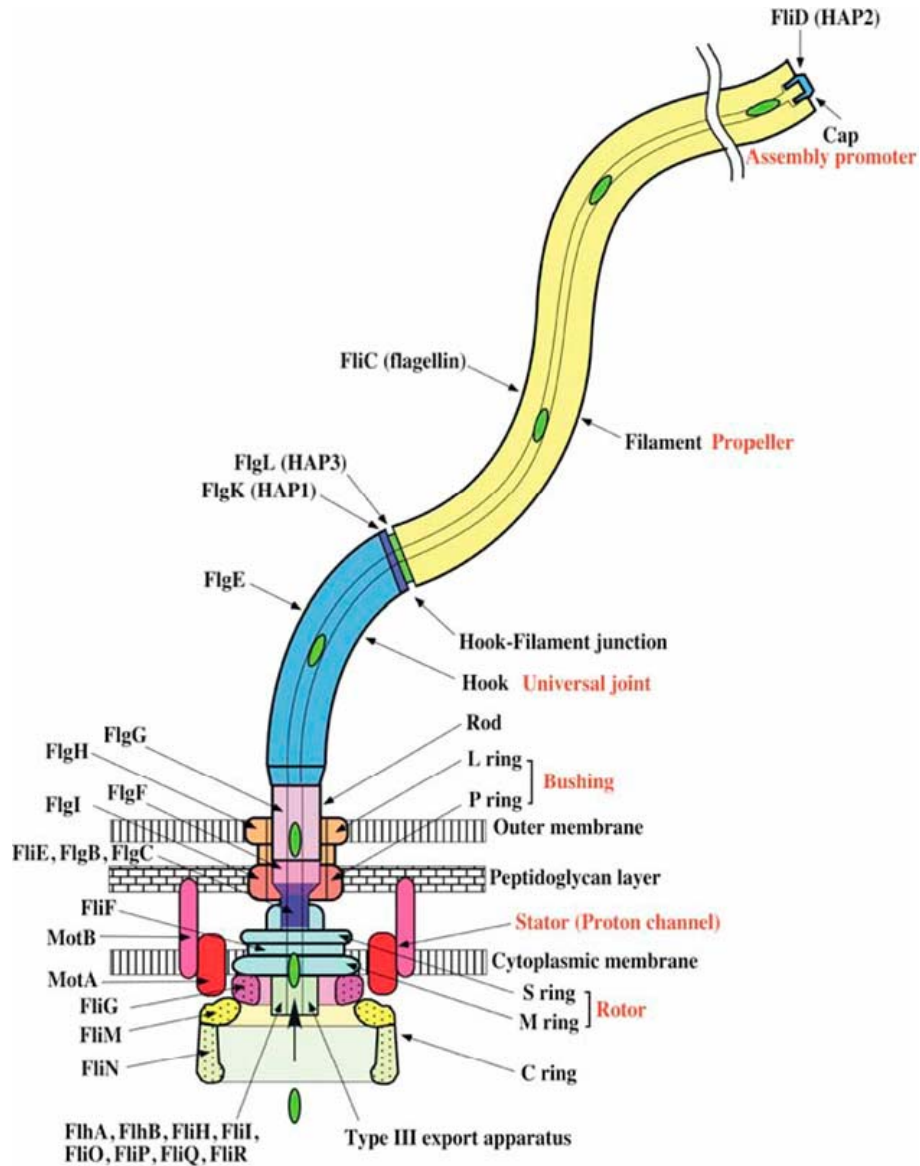


Figure 1-3 Schematic diagrams showing the overall architecture of the bacterial flagellum. Different colours represent different protein components. The filament growth occurs by polymerization of flagellin below the cap (figure adapted from Yonekura *et al.* 2002).

The inward assembly involves the formation of the C-ring, which is also called the switch complex, made of FliG, FliM and FliN (**Figure 1-3**), in the cytoplasmic space. The switch complex regulates the reversal frequency of the motor rotation and is also involved in torque generation. The type III protein export apparatus, which is homologous to those that enable pathogenic bacteria to secrete virulence factors (Kubori *et al.* 1998), is then formed within the C-ring, enabling the export of the flagellar axial proteins through its central channel. The lateral assembly involves the MotA/MotB complex (**Figure 1-3**) in the inner membrane, where it forms a proton channel. This complex acts as the stator by anchoring the periplasmic domain of MotB to the peptidoglycan layer.

The outward assembly (**Figure 1-4**) of the flagellar axial structure, which is the major process in the formation of the flagellum in terms of the mass fraction involved, proceeds at the distal end, as it was initially found for filament growth. The L-P ring (**Figure 1-3**) assembly is an exception, in which the subunit proteins, FlgH and FlgI (**Figure 1-3**), assemble in the outer membrane and peptidoglycan layer, respectively, to form a bushing. For all axial structure formation, the type III protein export system selectively binds and translocates flagellar axial proteins into the central channel of the flagellum by using the energy of ATP hydrolysis (Fan *et al.* 1997; Minamino and Macnab 1999). The axial proteins construct the rod, the hook, the hook-filament junction and the long filament in that order. The rod, composed of five proteins, is connected to the FliF ring (**Figure 1-3**) at its proximal portion with the hook at its distal end, and traverses the inside of the L-P ring. FlgE assembles (**Figure 1-3**) in a helical manner to form the hook. In most species examined, the hook is a short curved structure slightly thicker than the

filament (about 20nm) (Berry and Armitage 1999) and showing a high bending flexibility, which works as a universal joint.

A capping complex made of FlgD (**Figure 1-3**) is attached at the distal end of the hook until it grows up to a length of about 55 nm. Then the FlgD cap falls off the tip of the hook (Ohnishi *et al.* 1994) and is replaced by FlgK, and then FlgL and FliD are transported and bound at the distal end in that order. FlgK, FlgL and FliD are also called hook-associated proteins, HAP1, HAP3 and HAP2, respectively, because the hook-HAP1-HAP3-HAP2 complex is formed momentarily before the initiation of flagellin assembly into the long helical filament (Homma and Iino 1985).

Flagellin travels a long way through the narrow tunnel, only 3 nm in diameter but up to 10–15 μm long, to the distal end of the growing flagellum, which assembles with helical symmetry into the mechanically stable filamentous structure to function as a helical propeller (**Figure 1-4**). The filament cap made of HAP2 is always attached at the distal end, promoting the efficient assembly process (Yonekura *et al.* 2002). The cap has five legs that leave room for only one flagellin subunit at a time, and it counter rotates to accommodate insertion of additional subunits, one after another (Berg 2003).

1.2.2 The Bacterial Flagellar Filament

The flagellar filament has a tubular structure. Varying with the species, the flagellar filament is about 12-25 nm in diameter but grows up to a length of around 15 μm (Kamiya and Asakura 1976b). The central channel through the flagellar filament is about 2.5-3.0 nm (Namba and Vonderviszt 1997).

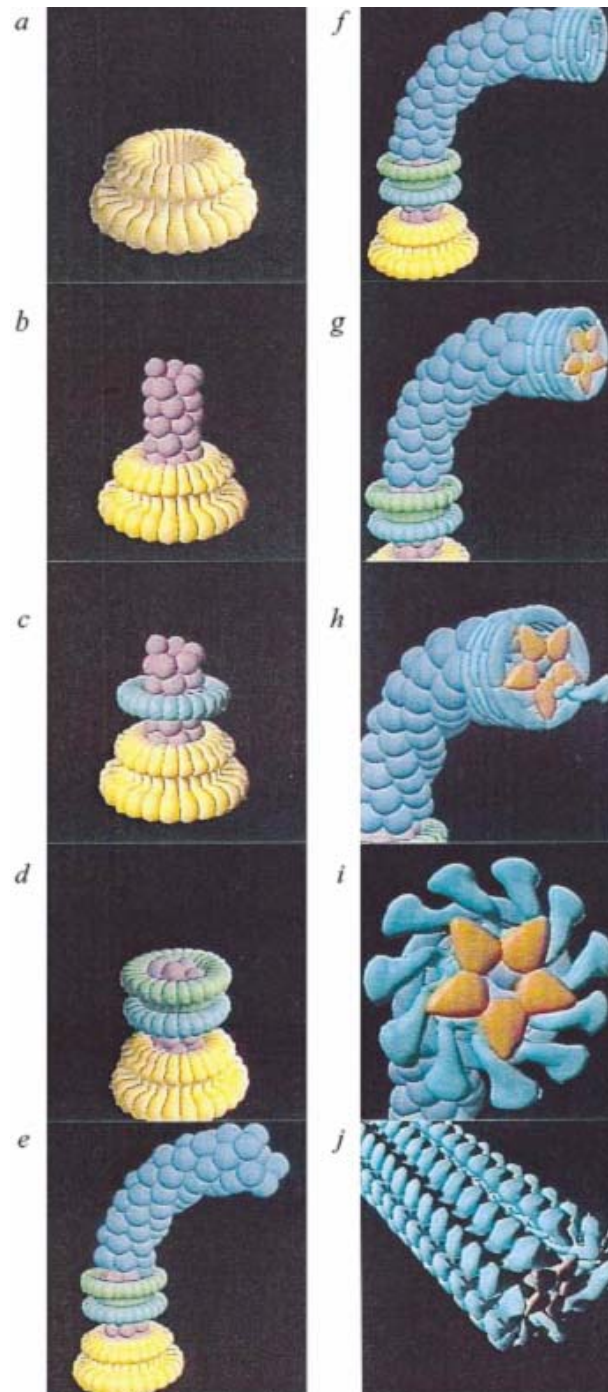


Figure 1-4 Outward assembly pathway of the flagellum. It starts from (a) the FliF ring, followed by sequential addition of (b) the rod, (c) P-ring, (d) L-ring, (e) hook, (f) HAP1 and HAP3, (g) HAP2, (h) a flagellin subunit, (i) 10 flagellin subunits, and (j) filament formation (figure adapted from Namba and Vonderviszt 1997).

1.2.2.1 Bacterial Flagellin

The flagellar filament is generally composed of over 10 000 copies of a single protein, flagellin, with a molecular mass varying from 25 to 60 kDa depending on the species. Some species may have more than one flagellin but the proteins are usually closely related (Berry and Armitage 1999).

Flagellin consists of four linearly connected domains labelled D0, D1, D2 and D3, which are arranged from the inside to outside of the filament (**Figure 1-5 a**). The N-terminal chain starts from D0, going through D1, D2 and reaches D3, and then comes back through D2 and D1, and the C-terminal chain ends in D0. Although all three domain connections are formed by pairs of short antiparallel chains, the one that connects domains D0 and D1 is longer than the other two, and therefore it is called the spoke region. The overall shape of flagellin looks like an upper case Greek gamma (Γ) with a vertical dimension of about 14.0 nm and a horizontal dimension of about 11.0 nm.

Flagellin has been found to be very susceptible to even a mild proteolytic treatment. When digested with trypsin or subtilisin, both termini of flagellin from *Salmonella typhimurium* (51.5 kDa) were found to be quickly degraded, resulting in a compact metastable product of 40 kDa. In contrast, the central region of the molecule is quite stable against proteolysis, probably because it is composed of compact structural units (Namba and Vonderviszt 1997).

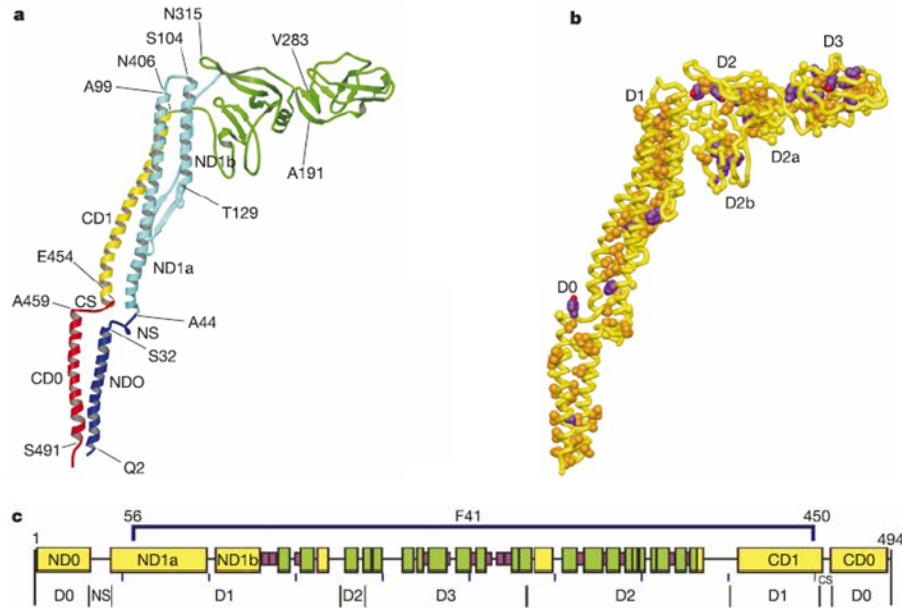


Figure 1-5 The C α backbone trace, hydrophobic side-chain distribution and structural information of flagellin. (a), Diagram of the C α backbone. The chain is coloured as follows: residues 1–44, blue; 44–179, cyan; 179–406, green; 406–454, yellow; 454–494, red. (b), Distribution of hydrophobic side chains, mainly showing hydrophobic cores that define domains D0, D1, D2a, D2b and D3. Side-chain atoms are coloured as follows: Ala and Met, yellow; Leu, Ile and Val, orange; Phe, Tyr and Pro, purple (carbon) and red (oxygen). (c), Position and region of various structural features in the amino acid sequence of flagellin. Shown are, from top to bottom: the secondary structure distribution with α -helix in yellow, β -structure in green and β -turn in purple; the well conserved amino-acid sequence in red and variable region in violet (figure adapted from Yonekura *et al.* 2003).

1.2.2.2 Intersubunit Interactions in the Filament

The filament is a tubular structure composed of 11 protofilaments (**Figure 1-6**) with their lateral disposition staggered axially by about half a subunit, and therefore approximately 5.5 subunits exist in one turn of the one-start helical path that goes through all the subunits (Yonekura *et al.* 2002).

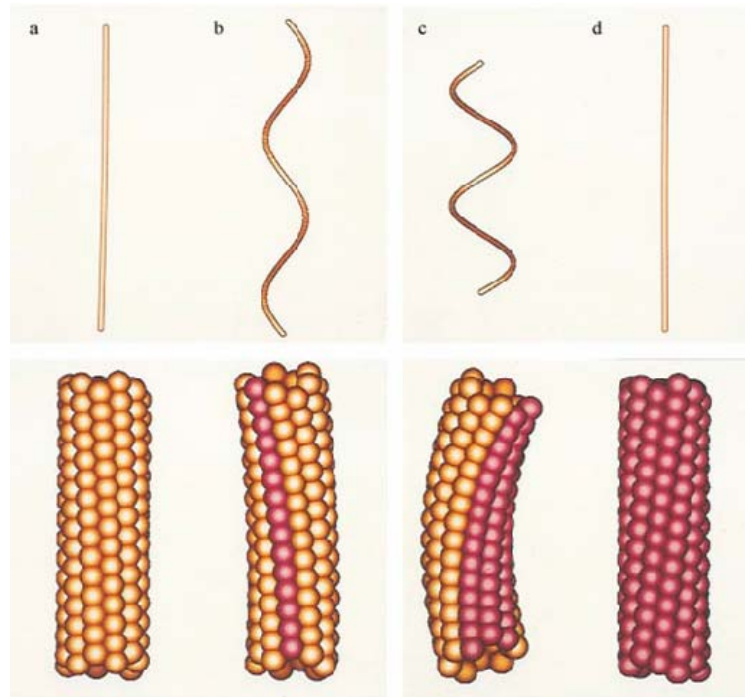


Figure 1-6 Polymorphic model of the filament. The top panel shows morphology of the filaments and the bottom panel shows the subunit arrangements within a short segment. The filaments are named: (a) L-type straight, (b) normal, (c) curly and (d) R-type straight. The two subunit colours represent the two distinct states of flagellin. The supercoil in (b) is left-handed and that in (c) is right-handed (figure adapted from Namba and Vonderviszt 1997).

The subunits pack in two different ways: The subunits in ‘short’ protofilaments (R-type) are closer together than the subunits in ‘long’ protofilaments (L-type) (**Figure 1-6, Figure 1-7**). R and L refer to the direction of twist. If both types are present at the same time, the filament has curvature as well as twist and is helical, with the short protofilaments running along the inside of the helix (Berg 2003). Mechanical strain energy is minimized when short protofilaments are next to short protofilaments and long protofilaments are next to long protofilaments, leading to 12 possible conformations, 2 straight (all short or all long) and 10 helical (Berg 2003). Filaments can be made to switch between these different helical

conformations, which is driven by motor switching or by changes in either the viscous forces on the filament or pH (Berry and Armitage 1999).

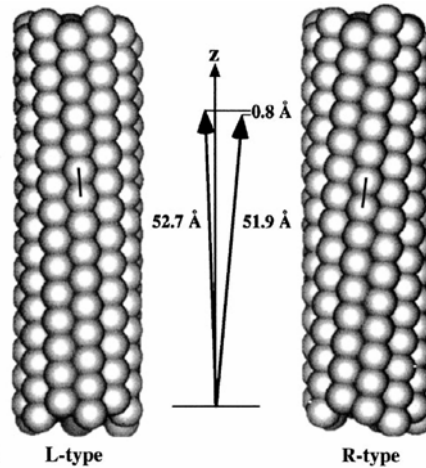


Figure 1-7 The surface lattice of L- and R-type straight flagellar filaments. The spacing between flagellin subunits along an 11-start helix (a protofilament) of the R-type is 0.08 nm less than between corresponding subunits of the L-type. L and R refer to the handedness of the filament twist. The distances are measured at a radius of 4.5 nm and are shown magnified in the middle of the drawing (figure adapted from Berg 2003).

The structure of the filament has been analyzed at around 10 Å resolution by **electron cryomicroscopy** and helical image reconstruction (Mimori *et al.* 1995; Morgan *et al.* 1995). The density map shows a densely packed core region out to a radius of about 60 Å, a central channel with a diameter of about 30 Å, and well-resolved outer parts that slew out to a radius of 115 Å. There are two radial regions of high density in the core region, one from 15 to 30 Å (Domain D0) and the other from 35 to 60 Å (Domain D1). These two regions form a concentric double tubular structure, and the inner and outer tubes are connected by radial spoke-like densities. The outer part also consists of two domains: domain D2 has

the shape of a vertical column; domain D3 is a projection that extends out from the upper part of the vertical column. Domains D2 and D3 consist of mainly β -strands and domain D1 contains three long α -helices paired with a β -hairpin (Yonekura *et al.* 2002). The subunits are closely packed in the core region and it is not possible to determine the subunit boundary there. In the outer region, however, the subunits are well separated from each other (Namba and Vonderviszt 1997).

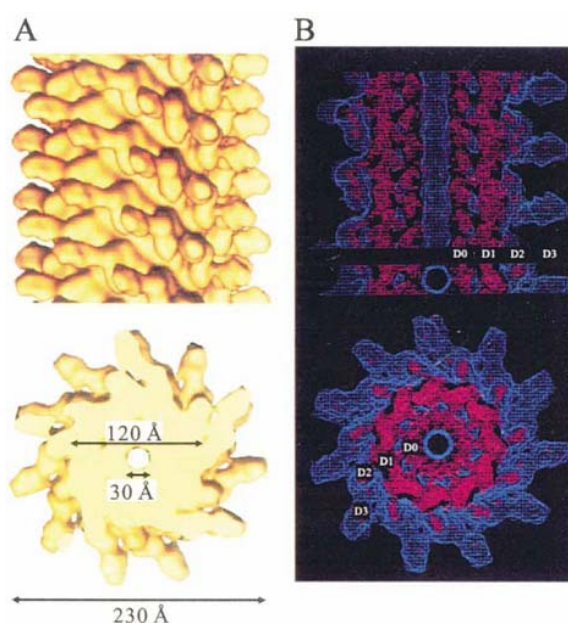


Figure 1-8 Three-dimensional density map of the flagellar filament (R-type straight filament), calculated by including data up to 9 Å. (A) Solid surface representation of a side view with the distal end up (upper panel) and the end-on view from the proximal end (lower panel). (B) Wire frame representation of a 50 Å thick cross section and a 30 Å thick longitudinal section. The directions of views are the same as in (A). Counter lines in blue represent approximately the correct volume of the filament, and those in red show a density level twice as high as that in blue (figure adapted from Yonekura *et al.* 2002).

Domains D0 and D1 make intimate intersubunit interactions, both axially and laterally. Thus, the N- and C-terminal chains of flagellin are essential for filament assembly.

Most of the intersubunit interactions found within the outer tube are polar–polar or charge–polar, and contributions of hydrophobic interactions are relatively small, whereas those found within the inner tube and between the inner and outer tubes are mostly hydrophobic, contributing to the high stability of the filament structure.

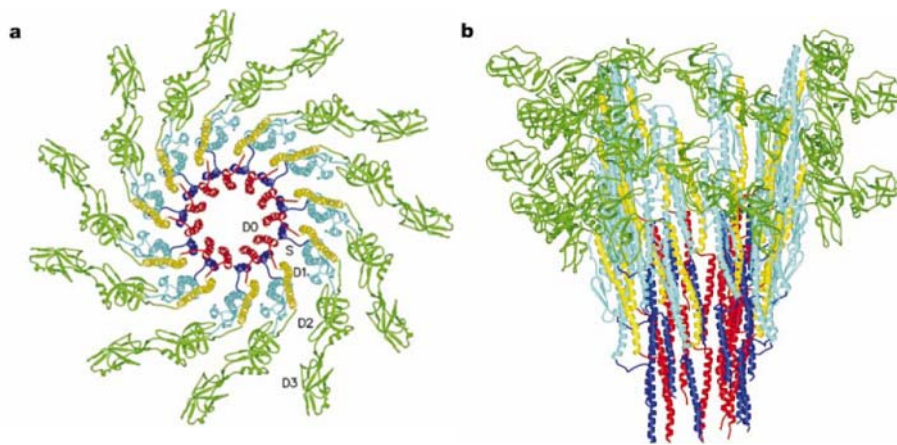


Figure 1-9 Ribbon diagram of the C α backbone of the filament model in stereo view. (a), End-on view from the distal end of the filament. Eleven subunits are displayed. (b), Side view from outside the filament. Three protofilaments on the far side have been removed for clarity. Top and bottom of the side view image correspond to the distal and proximal ends of the filament, respectively. The chain is colour coded as in **Figure 1-5** (a) (figure adapted from Yonekura *et al.* 2003).

1.2.2.3 Transformations of Flagellar Filaments *in vitro*

For chemotaxis and thermotaxis, the swimming pattern of bacteria such as *Salmonella* and *Escherichia coli* alternates between ‘run’ and ‘tumble’; a run lasts

for a few seconds and a tumble for a fraction of second. During a run, the motor rotates anticlockwise (as it is viewed from outside the cell), and several flagellar filaments with a left-handed helical shape form a bundle and propel the cell. A tumble is caused by quick reversal of the motor to clockwise rotation (Larsen *et al.* 1974), which produces a twisting force that transforms the left-handed helical form of the filament into a right-handed one (Macnab *et al.* 1977; Turner *et al.* 2000), causing the bundle to fall apart rapidly. The separated filaments act in an uncoordinated way to generate forces that change the orientation of the cell. Thus, the structure of the flagellar filament and its dynamic properties have an essential role in bacterial taxis.

Reconstituted *Salmonella* flagellar filaments were found by dark field light microscopy to undergo reversible transformations at both acidic and alkaline pH (Kamiya and Asakura 1976). Flagellar filaments from SJ670 strain are left-handed helices with a pitch of 2.3 μm (normal type) at neutral pH. When, however, the pH of the solution is lowered to 4.7, they are discontinuously transformed into closed-coils with a pitch of 0.5 μm and a diameter of 1.2 μm , and a further lowering of the pH converts these coiled flagellar filaments into so-called curly ones, which are right-handed helices with a pitch of 1.1 μm . When the pH was increased from 7 to 12.5, flagellar filaments from strain SJ670 were found to rapidly transform from the normal type to a left-handed close-coil (coiled type) or to two types of right-handed helices with a pitch of 1.0 or 0.9 μm . Kamiya and Asakura concluded that the pH is an important factor in the control of flagellar transformation.

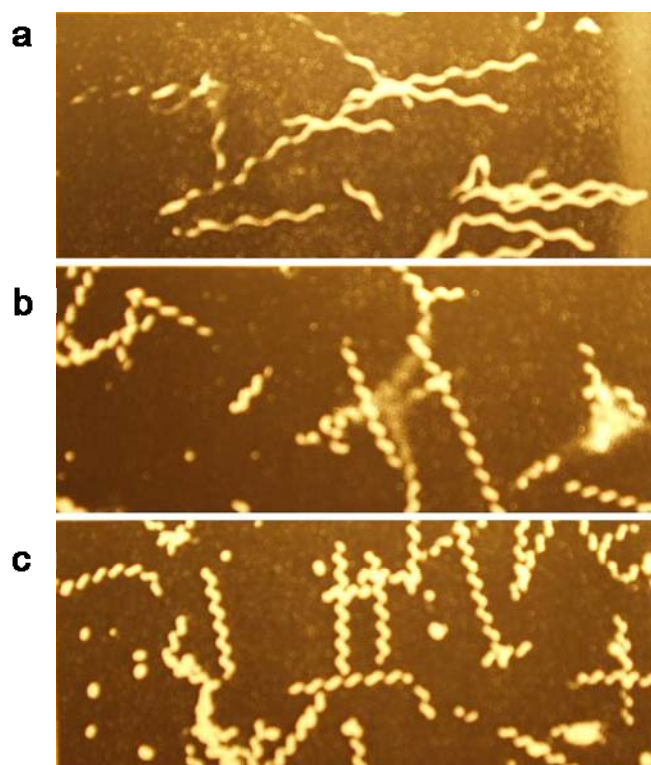


Figure 1-10 Dark field light micrographs of *Salmonella* flagellar filaments. (a) Normal form found at pH 7.0 (1mM potassium phosphate buffer and 100 mM KCl) with pitch = 2.3 μm ; (b) curly form at pH 4.1 (0.1 M NaCl, 1 mM acetic acid and 1mM sodium acetate, pH value was adjusted by the addition of 1 M HCl or 1 M NaOH) with pitch = 1.1 μm ; (c) curly form at pH 12.0 (100 mM KCl, pH value was adjusted by the addition of 1M KOH or 1 M HCl) with pitch = 1.0 μm (figure adapted from Kamiya and Asakura 1976).

1.2.3 Applications of Bacterial Flagellar Filaments

The flagellar filaments can be naturally produced by bacteria very quickly (see section 2.2.1). They can be easily removed from the cells by mechanical shearing. The flagellin has conserved regions at the N- and C-termini, that are required for anchoring of the flagellin into the nanotubular structure. However, the central region which is partially displayed on the filament surface is variable. The single gene encoding flagellin can be easily engineered to allow the surface display of

inserted epitopes along the length of the filament. Woods and co-workers (2007) functionalized *Escherichia coli* FliC flagellin to form tailored nanotubes capable of binding single types or pairs of ligands, including divalent cations, fluorescent antibodies, or biotin-avidin-linked moieties such as ferritins.

Kumara and co-workers (2006) produced cysteine-containing FliTrx to form bundles of functionalized flagellar nanotubes (**Figure 1-11**). Later (2007) they also demonstrated that the peptide loop modified flagella nanotubes could be used as scaffolds for the generation of ordered array of metal nanoparticles or uniform nanotubes (**Figure 1-12**). FliTrx was genetically modified to display designed histidine, arginine-lysine, and aspartic acid-glutamic acid peptide loops on the solvent-accessible outer domain region. The resulting flagellin monomers were self-assembled to obtain flagellar nanotubes in which the peptide loops were 5 nm apart. These flagellar nanotubes were equilibrated with solutions of various metal ions (Co(II), Cu(II), Cd(II), Ag(I), Au(I), and Pd(II)). Controlled reduction of these metal ions yielded ordered arrays of nanoparticales or nanotubes, and in some cases, extensive aggregation resulted in the formation of metal nanotube bundles.

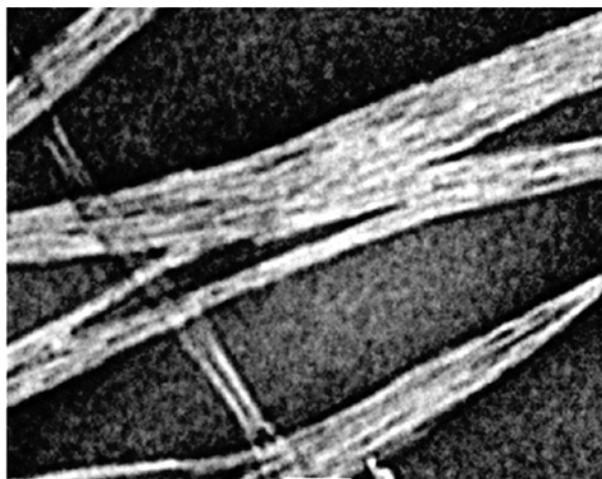


Figure 1-11 TEM images of disulfide cross-linked Cys-loop flagella bundles stained with 2% phosphotungstic acid (pH 7.5) (scale bar 100nm) (figure adapted from Kumara *et al.* 2006).

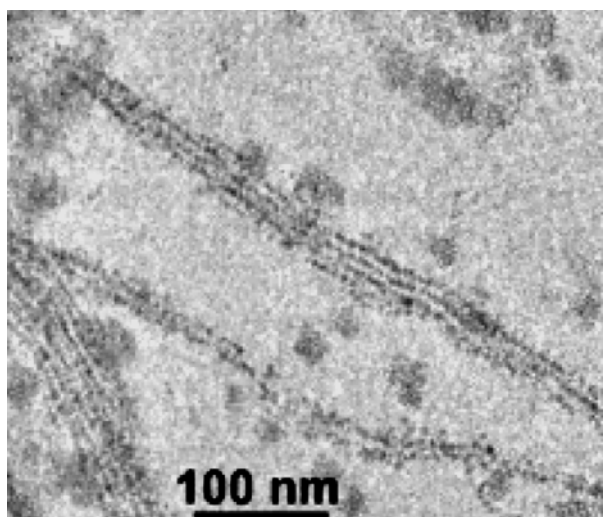


Figure 1-12 TEM images of gold nanoparticles that were synthesized by reduction of Au(I) on a histidine loop peptide flagella scaffold (figure adapted from Kumara *et al.* 2007).

1.3 Amyloid Fibrils

1.3.1 Protein Misfolding

1.3.1.1 Protein Misfolding and Diseases

Amyloid is an insoluble form of protein that results when a normally soluble protein converts via a **self-assembly process** to form a well-defined fibrillar structure. Amyloid accumulates in a variety of organs including the liver, spleen, and brain. Amyloid fibrils underlie a large family of clinical disorders, and the term amyloidosis is used to describe the clinical conditions with which amyloid is associated (Chiti and Dobson 2006). Examples of amyloidogenic peptides and proteins are listed in **Table 1-1**.

Lysozyme (**Figure 1-13 (a)**), for example, is a 129-amino-acid **residue enzyme** which catalyzes hydrolysis of 1,4-beta-linkages between N-acetylmuramic acid and N-acetyl-D-glucosamine residues in peptidoglycan and between N-acetyl-D-glucosamine residues in chitodextrins. The molecular weight of lysozyme is approximately 14.7 kDa. Lysozyme is present in a number of secretions such as saliva, tears and mucus. Large amounts of lysozyme can also be found in egg whites. Lysozyme's catalytic activity is non-specifically targeted to the bacterial cell membranes and related with general non-specific organism defence. Human lysozyme has been shown to form amyloid fibrils in individuals suffering from non-neuropathic systemic amyloidosis (Krebs *et al.* 2000).

Peptide/protein	Conditions of fibrillation	Properties of the aggregate/fibrils	Remarks
Poly(L-lysine), poly(L-threonine), poly(L-glutamic acid)	65 °C and charge depleting pH (alkalic for K, acidic for E)	From straight, unbranched to short and twisted	Main chain interactions promote aggregation
Poly(L-lysine)+ poly(D-lysine),	Mixing at room temp. and alkalic pH	Highly distorted	Racemic fibrils form due to increase in water ΔS
FF ^a	Precipitation upon dilution with water	Regular “empty” nanotubes	Form “nanowires” when filled with Ag atoms
KVVE, KFFE ^a	Long incubation at 37 °C, neutral pH	Bundles resembling in vivo deposits	Charges compensated in the antiparallel alignment
(DPKG) ₂ -(VT) ₃ -GKGDPPKPD-NH ₂ ^a	Spontaneous fibrillation at 25 °C	Sequence-dependent morphologies	Monomers and early fibrils are soluble
Alzheimer β -peptide fragments	Aggregation dependent on pH	CD spectra same as for in vivo deposits	The pH-range parallels in vivo conditions
Oxidized glutathione (GSSG) ^a	Aqueous solutions of DMSO, DMF, MeOH	Thick, 75 nm in diameter fibrils	Network with β -sheet like motive traps solvent
Cyclic octa-peptides alternating D/L amino acids	Precipitation at acidic pH in the presence of cosolvent	Fibrils 1.5 nm thick with an internal diameter 0.7–0.8 nm	Open-ended “nanotubes” with a regular β -sheet like motive
Bovine serum albumin	Sonification at room temperature	Heterogeneous fibrils, 20 nm thick	Possible role of free radicals in the aggregation
Antifreeze protein of winter flounder	Repetitive freezing–thawing cycles.	Short, 5 nm in diameter	Ice-binding may trigger the fibrillation
C11A/C14A mut. cytochrome <i>c</i> ₅₅₂	Incubation at 25 °C, neutral pH	Typical fibrils are 6–13 nm thick	C11A/C14A substitution destabilizes <i>holo</i> -protein
Horse <i>apo</i> -myoglobin	A day-long incubation at 65 °C, pH 9	Fibrils are unstable above 65 °C	Amyloidogenesis requires complete unfolding
Bovine insulin	Hours-long incubation at 65 °C, pH 2	Fibrils associated in spherulites	Characteristic optical properties
Tetramerization domain p53 protein	Gradual heating up to 95 °C, pH 4	Straight and curly forms 1–2 nm thick	Amyloid disassembles above pH 8.5
Transthyretin	3.5 kbar pressure, at 37 °C, neutral pH	Formed after depressurization	Non-native aggregation-prone tetramers formed
Hen egg white lysozyme	2–5 M guanidine HCl, 50 °C, neutral pH	Twisted, approx. 13 nm thick	Denaturant concentration within range of 2 and 5 M
Yeast prion protein Ure2	Shaking at 37 °C, pH 8	Straight fibrils, 4–8 nm in height (AFM)	Highly heterogeneous samples
Prion proteins: Human PrP(90-231), Mouse PrP (89-230)	Shaking at 37 °C, at pH ranging from 3.7 to 7.2	Fibrils at neutral pH shorter than those formed at pH 3.7	Fibrillation enhanced by homologous seeding (Hu→Hu, Mo→Mo)

^a Peptide names decode amino acid sequence according to the one-letter system.

Beta2-microglobulin (**Figure 1-13 (b)**) which belongs to the immunoglobulin superfamily, is known to aggregate into amyloid that deposit at joint spaces in patients on long-term hemodialysis, a disease known as dialysis-related amyloidosis (DRA) (Smith and Radford 2001; Manning *et al.* 2003).

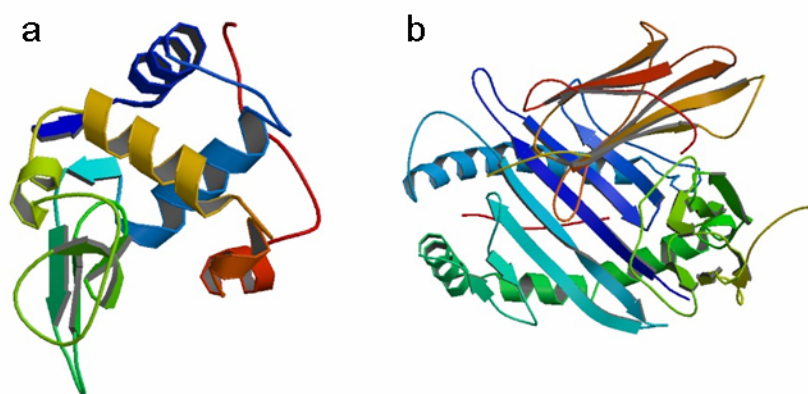


Figure 1-13 Stereo ribbon diagram of the structure of (a) lysozyme (b) beta2-microglobulin (www.pdb.org ID: 133l. Harata *et al.* 1993; ID: 1a1m. Smith *et al.* 1997).

1.3.1.2 Energy Landscape of Protein Folding

A typical energy landscape diagram of protein folding is displayed in **Figure 1-14**. The unfolded polypeptide chain gradually progress through various levels of organization that ultimately lead to the energetically stable folded native state (Dobson *et al.*, 1998). The nature of this energy landscape is influenced by features such as the protein sequence and the conditions under which folding occurs. Therefore, changing the conditions under which a protein folds, as in a disease state or as in the laboratory, can result in local energy minima; and an energy barrier may be created that halts continued folding towards the native state.

The increasing populations of these partially folded proteins may lead to a self-association process whereby they become “trapped” in an aggregated, non-native form.

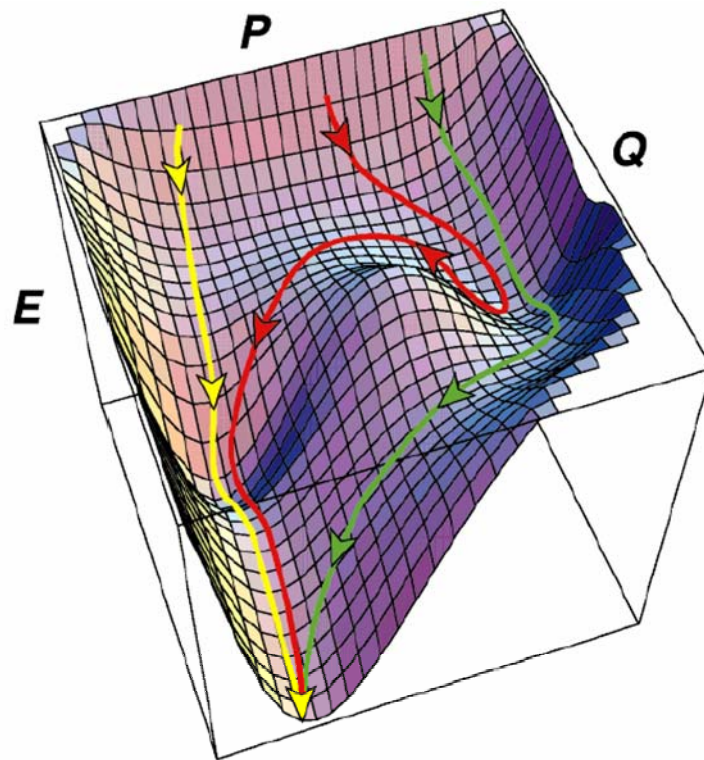


Figure 1-14 The estimated energy landscape diagram based on data for the folding of lysozyme. Several possible folding pathways are shown: a fast folding route (yellow), a slow folding route involving an energy barrier (green), and a slow folding route that returns to a less folded state and then joins the fast folding route (red). E refers to energy, P is a measure of the available conformational space, and Q is the fraction of native contacts (figure adapted from Dobson *et al.* 1998).

The formation of amyloid fibrils reflects the conformational struggle of polypeptide chains to reduce their surface accessible area, to saturate hydrogen

bonding, and to reach an alternative non-native free energy minimum (Dobson *et al.* 1998).

1.3.1.3 Structure of Amyloid Fibrils

Despite the diverse range of proteins that are involved in amyloid related diseases, all of which have unique native folding states, they are found to have extremely similar final morphologies in their misfolding states. The generic structure of amyloid fibrils has been revealed in some detail; however, the exact molecular conformation and supramolecular organization still needs to be determined. Perutz and co-workers (2001) proposed that amyloid fibrils are nanotubes with central water-filled cavity.

A generally accepted fibrilization pathway is as follows: first, the globular proteins partially unfold under certain conditions and self-assemble into protofilaments; the protofilaments then intertwine with each other into mature fibrils (Ban *et al.* 2006; Chamberlain *et al.* 2000; Khurana *et al.* 2003; Makin *et al.* 2005).

In laboratories, amyloid fibrils are usually produced by exposing proteins to mildly denaturing conditions, such as low pH or elevated temperatures. The exposure to denaturing conditions allows the peptide backbone to be accessible to form the interchain hydrogen bonds associated with amyloid fibrils (Dobson *et al.* 1998).

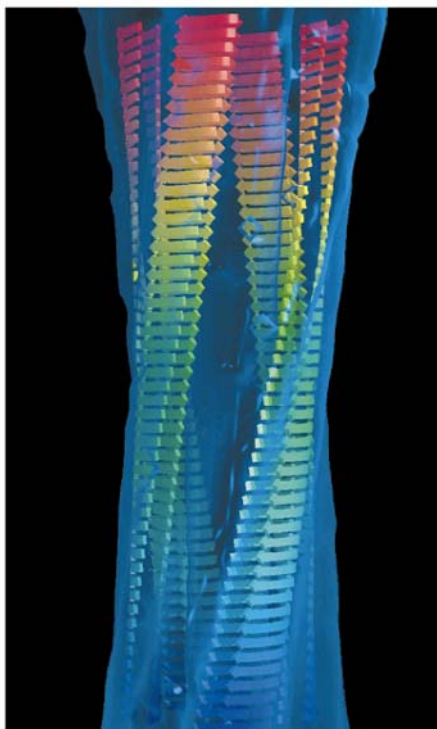


Figure 1-15 A molecular model of an amyloid fibril grown from an SH3 domain. The fibril consists of four protofilaments that twist around one another to form a hollow tube. Each protofilament is assembled through β domain (figure adapted from Dobson 1999).

Based on AFM analysis of the morphology of fibrillar species formed during amyloid fibrillization processes, Khurana and co-workers (2003) proposed a general model for the assembly of protein fibrils (**Figure 1-16**). Insulin fibrils were formed in vitro by stirring the protein in an acid solution (pH 1.6). Under those conditions, insulin fibrils were found to reach maturity after 4 hours of incubation. During the fibrillization process, protofilaments (1.2 ± 0.3 nm in diameter) and protofibrils (1.9 ± 0.3 nm in diameter) were observed. Two sizes of mature fibrils were also observed: a smaller fibril of 3.0 ± 0.4 nm in diameter, and a larger fibril of 4.8 ± 0.4 nm in diameter, which they identified as types I and II fibrils, respectively. They suggested that protofilament pairs intertwine with each other to

form protofibrils, and two protofibrils then intertwine to form a type I fibril. A type II fibril is formed by winding of two type I fibrils.

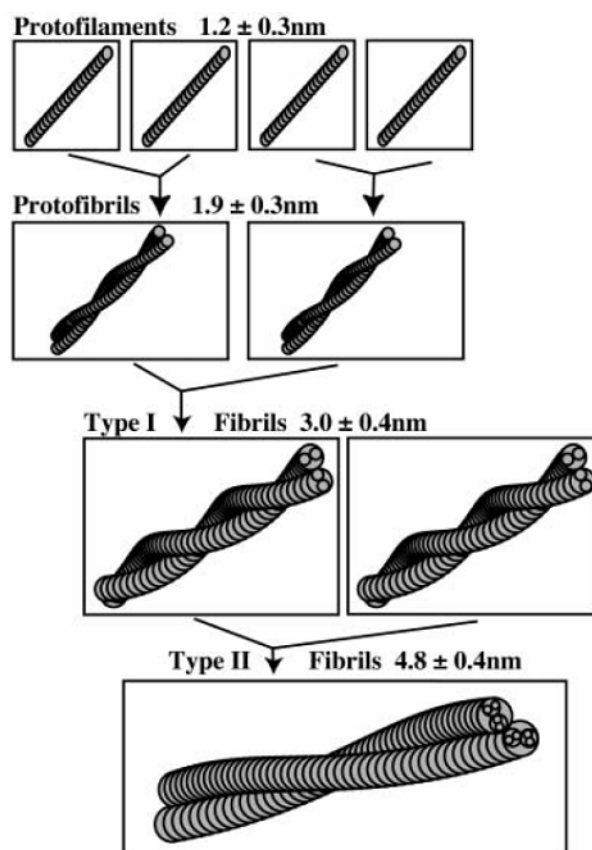


Figure 1-16 Khurana's model for the hierarchical assembly of insulin into amyloid fibrils. Protofilament pairs wind together to form protofibrils, and two protofibrils wind to form a type I fibril. Type II fibrils are the result of winding of type I fibrils (figure adapted from Khurana 2003).

Another AFM study carried out by Jansen and co-workers (2005) on insulin aggregates suggested that, in addition to the hierarchical pathway of fibrilization, there was an alternative self-assembly route leading to insulin fibrils which involved the lateral interaction of early, prefibrillar forms with protofilaments.

The nature of multipathway fibrilization resulted in a more complex morphological variety.

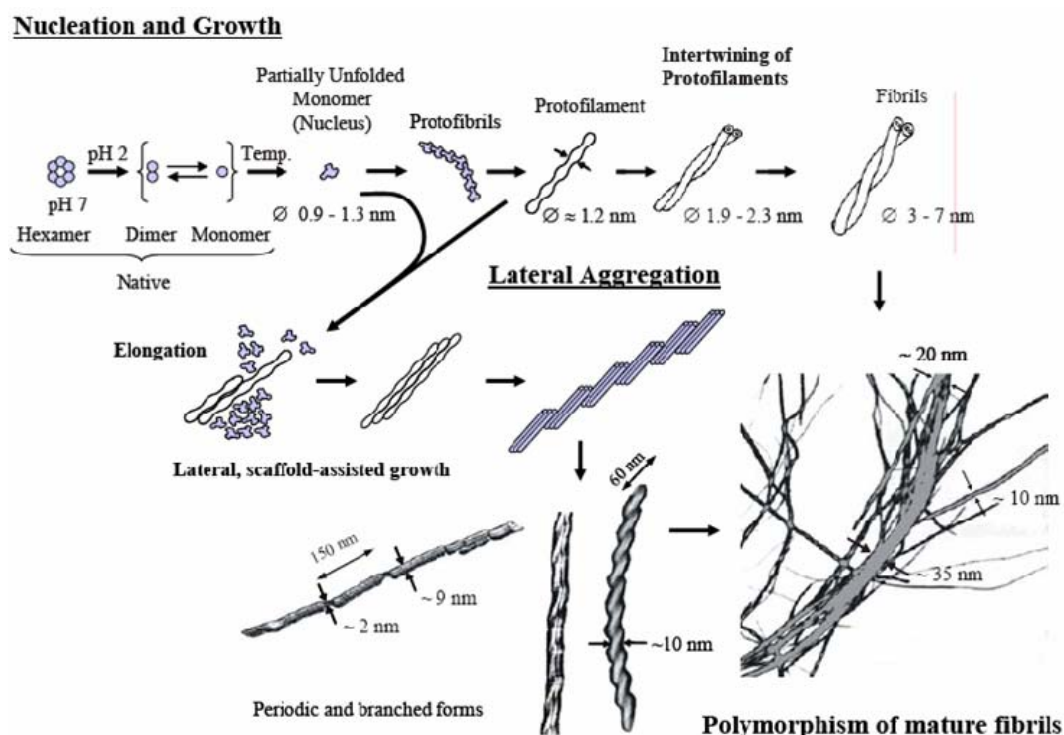


Figure 1-17 A general scheme of the multipathway fibrilization of insulin. Insulin hexamers undergo monomerization at low pH and then form protofilaments which then intertwine with each other to form mature fibrils. The lateral interaction of early, prefibrillar forms with protofilaments, followed by the lateral association of protofilaments, is an alternative self-assembly route. Under the given conditions, insulin fibrilization proceeds through both pathways (figure adapted from Jansen *et al.* 2005).

An interesting circular morphology of insulin amyloid formed under high hydrostatic pressure was discovered by Jansen and co-workers (2004) (**Figure 1-18**). While high pressure was found to prevent insulin aggregation, the protein nevertheless was able to slowly form amyloid with this unprecedented circular

morphology. Jansen suggested that at high pressure, the fibril tends to bend in one direction throughout the elongation process.

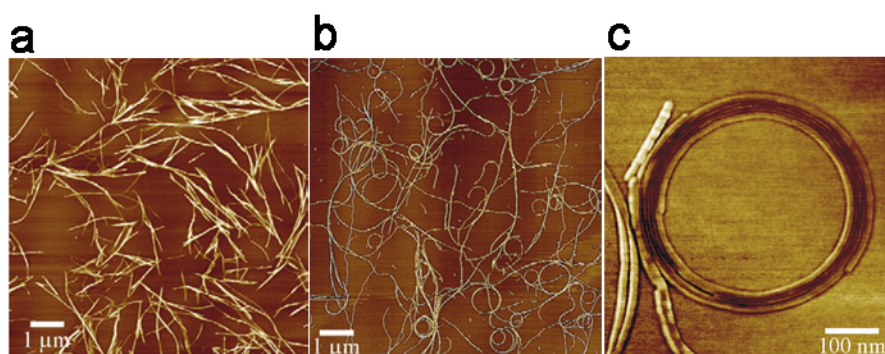


Figure 1-18 AFM height images of insulin amyloid. (a) Control sample, 0.5% (w/w) of bovine insulin in water, pH adjusted to 1.9, was kept at ambient pressure and 60 °C for 21 hours. (b) Insulin sample was kept at 60 °C for 20 hours after increasing the pressure to 1500 bar and kept for one hour after pressure-release. (c) High-resolution AFM images of the circular amyloid reveal its ultrastructural features (figure adapted from Jansen 2004).

Similar circular forms of insulin fibrils (**Figure 1-19**) were observed by Grudzielanek and co-workers (2005) when they were studying the solvational effects on the unfolding, aggregation and amyloidogenesis of insulin. Ethanol acts as an aggregation enhancer at low concentrations and an inhibitor at higher concentrations. The addition of concentrations as low as 5% (w/w) of ethanol was found to trigger the appearance of bent and circular fibrils, the diameter of which was typically 750-800 nm. The amount of circular forms reduced in 20% (w/w) ethanol and vanished completely at 40% (w/w) ethanol.

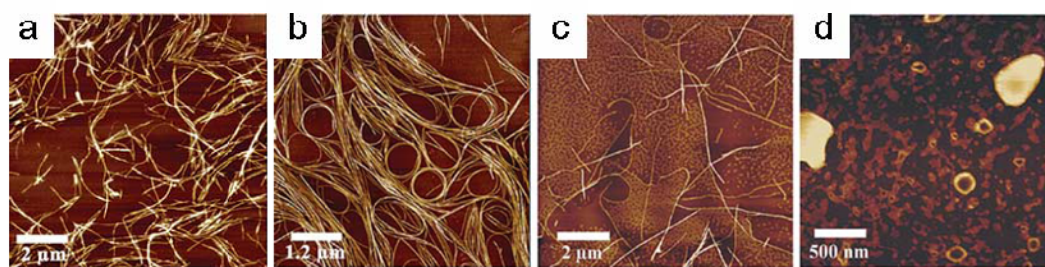


Figure 1-19 AFM images of 0.1% (w/w) insulin, aggregated at 60 °C for six days in: (a) water; (b) 5% (w/w) EtOH; (c) 20% (w/w) EtOH; (d) 40% (w/w) EtOH (figure adapted from Grudzielanek 2005).

Dzwolak (2006) reviewed the results of tuning amyloidogenic conformations through cosolvents and hydrostatic pressure, and proposed a hypothetical model of hyperbaric and solvational control of insulin amyloid polymorphism. He pointed out that although both native insulin and insulin amyloid are resistant to high pressure and the influence of cosolvents, the intermediate aggregation-prone conformations are susceptible to either condition. A lower void volume conformation was proposed to be favoured under high pressure. The persistent bending of a fibril towards one direction during its elongation to form circular morphology was proposed to suggest an anisotropic distribution of cavities within the ambient fibril.

1.3.2 Applications of Amyloid Fibrils

The well-ordered structure of amyloid fibrils confers stability at extremes of pH, temperature, or pressure; fibrillar structure is typically preserved in both aqueous and organic solvents. Amyloid fibrils are also resistant to proteolysis and dehydration (Gras 2007a; 2007b). All of these favourable properties, associated with the versatile modifiability of the peptides/polypeptides by chemically

introducing functional groups, enable amyloid fibrils to hold a great potential as biomaterials for nanotechnology and bionanotechnology.

Before commercial applications of amyloid fibrils in nanotechnology and bionanotechnology can be fully realised, a high degree of control of their properties needs to be achieved, which requires the further study of the relationship between the functionalization of the peptides/polypeptides and the characteristics of amyloid fibrils (Waterhouse and Gerrard 2004). Meanwhile, some recent attempts to exploit amyloid fibrils as biomaterials have been promising.

Scheibel and co-workers (2003) reported the use of self-assembling fibres to construct nanowire elements. Self-assembly of a prion determinant from *Saccharomyces cerevisiae*, the N-terminal and middle region (NM) of Sup35p, produced 10-nm-wide protein fibres. These NM fibres were stable under a wide variety of harsh physical conditions; and their length could be roughly controlled by assembly conditions in the range of 60 nm to several hundred micrometers. A genetically modified NM variant that presented reactive, surface-accessible cysteine residues was used to covalently link NM fibres to colloidal gold particles. These fibres were placed across gold electrodes, and additional metal was deposited by highly specific chemical enhancement of the colloidal gold by reductive deposition of metallic silver and gold from salts. The resulting silver and gold wires were ~ 100 nm wide (**Figure 1-20**). These biotemplated metal wires demonstrated the conductive properties of a solid metal wire, such as low resistance and ohmic behaviour (**Figure 1-21**). With such materials it should be

possible to harness the extraordinary diversity and specificity of protein functions to nanoscale electrical circuitry.

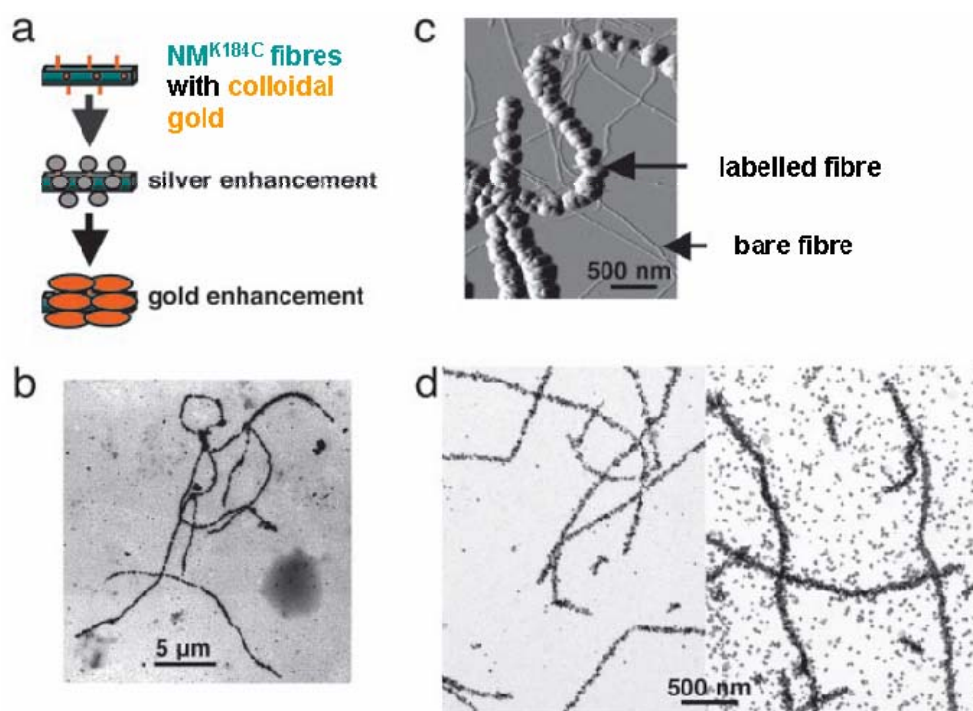


Figure 1-20 Gold and silver enhancement of NM fibres. (a) Illustration of silver and gold enhancements. Monomaleimido nanogold was covalently cross-linked to NM^{K184C} fibres and then fibres were gold-toned by enhancing with LI Silver and GoldEnhance LM. (b) TEM image of gold-toned fibres. (c) AFM height image of gold toned fibres with significant increase in height compared to bare fibres. (d) AFM height images of (left) gold-labelled fibres on Si₃N₄ subjected to 3 min of silver enhancement and 5 min of gold enhancement, leading to a fibre diameter of 50 ± 5 nm, and (right) fibres after 5 min of silver enhancement and 5 min of gold enhancement, leading to a fibre diameter of 100 ± 7 nm (Figure adapted from Scheibel *et al.* 2003).

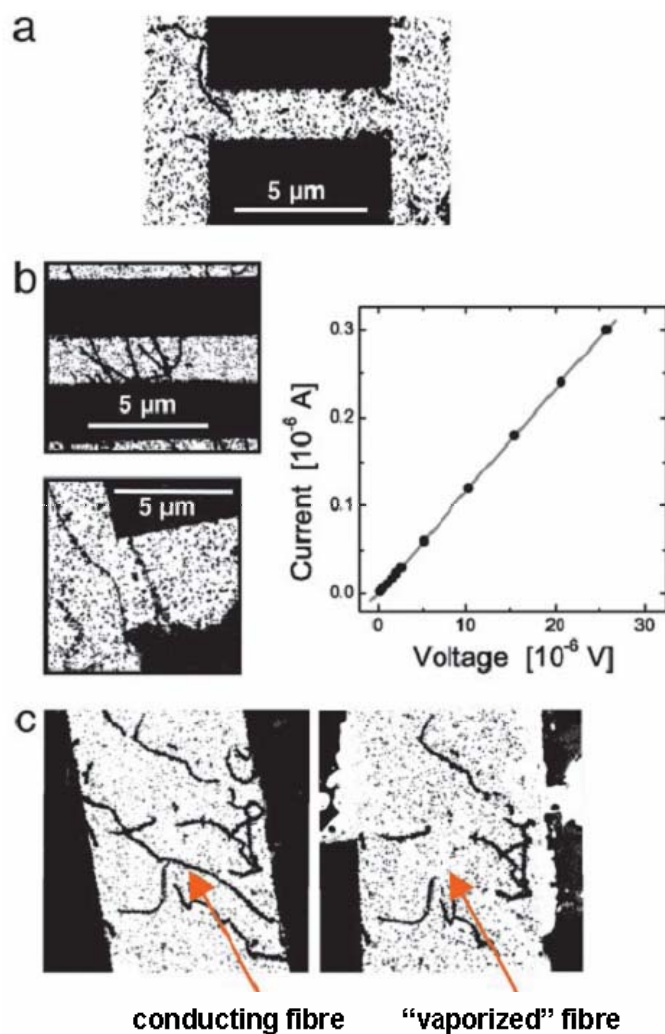


Figure 1-21 Electrical behavior of NM-templated metallic fibres. TEM images of gold- and gold-toned fibres randomly deposited on patterned electrodes. (a) Gold nanowires that did not bridge the gap between two electrodes did not conduct. (b) Gold nanowires that bridged the gap between two electrodes (left) exhibit linear I–V curves (right), demonstrating ohmic conductivity with low resistance of $R = 86 \, \Omega$ (the same for each). Such ohmic response is indicative of continuous, metallic connections across the sample. (c) In some experiments, after ramping up the voltage, reversing the scan direction no longer showed conductivity. Imaging revealed that the conducting nanowires were vaporized. Before (left) and after (right) conductivity measurement (figure adapted from Scheibel *et al.* 2003).

1.3.3 Diphenylalanine Nanotubes (FF Nanotubes)**1.3.3.1 Discovery and Synthesis of Diphenylalanine Nanotubes**

By comparing a number of structurally unrelated short functional fragments of amyloid-related polypeptides, Gazit (2002) noted a remarkable occurrence of aromatic residues. In many areas of chemistry and biochemistry, especially in self-assembly and molecular recognition, the attractive non-bonded interactions between planar aromatic rings, which are referred to as π - π interactions or π -stacking, play a central role. Gazit then speculated that the π - π interactions may provide energetic contribution as well as order and directionality in the self-assembly of amyloid structures. Bearing this in mind, in the spirit of looking for the simplest building blocks of bionanomaterials, Reches and Gazit (2003) discovered the self-assembly of diphenylalanine peptide (NH_2 -L-Phe-L-Phe-COOH, FF see **Figure 1-22**) into discrete and stiff nanotubes. They dissolved diphenylalanine peptide in 1,1,1,3,3,3-hexafluoro-2-propanol (HFIP) at high concentrations ($\geq 100\text{mg/mL}$) and then diluted into an aqueous solution with a final μM concentration range; a rapid assembly was observed. A stable analogue of the nanotubes composed of D-isomer amino acids (NH_2 -D-Phe-D-Phe-COOH) could also be prepared; but unlike those prepared from the L-isomer, these nanotubes were stable to proteolytic degradation.

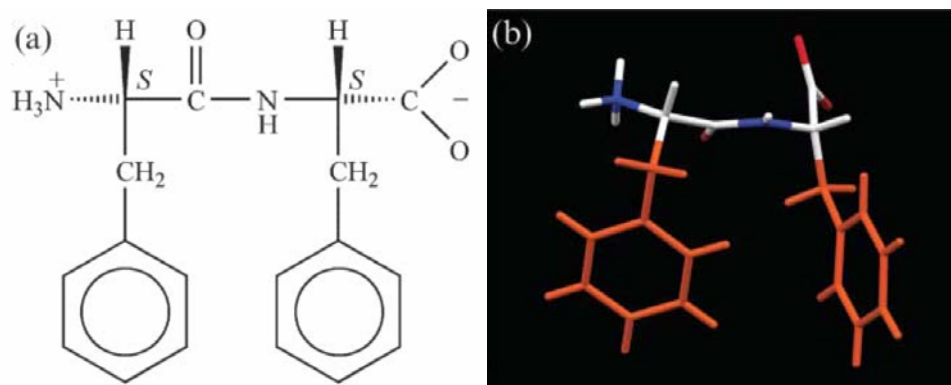


Figure 1-22 (a) Schematic structure of FF. (b) The molecular structure of FF from the single crystal structure determination. Side-chain atoms are shown in orange (figure adapted from Gorbitz 2001).

FF nanotubes synthesized by the Reches and Gazit (2003) method, were several micrometers in length and 50 to 300 nm in diameter. Song and co-workers reported (2004) another method which simplified the synthesis and made it more environmentally benign by omitting HFIP. In a typical synthesis, 10 mg of lyophilized peptide ($\text{HN}_2\text{-D-Phe-D-Phe-COOH}$) was dissolved in 5 mL water at 65 °C, and the sample equilibrated for 30 min and then gradually cooled to room temperature. Scanning Electron Microscopy (SEM) images showed that the nanotubes obtained using this procedure were 100 nm to 2 μm in diameter and could exceed 100 μm in length. Interestingly, when 0.1 mL of the nanotube mixture was diluted by adding 0.1 mL of water, vesicles were observed in addition to the nanotubes. Song suggested that these results indicated that the concentration of the peptide was a key factor in the formation of the nanotubes and that the HFIP was not critical for the self-assembly process.

1.3.3.2 Structures and Properties of diphenylalanine Nanotubes

Transmission Electron Microscopy (TEM) analysis with negative staining indicated that the structures of FF nanotubes were well-ordered elongated assemblies with no branching. Almost no amorphous aggregates were observed (<1%), which is in contrast to other peptide assemblies (such as amyloid fibrils) in which a mixture of ordered and aggregated structures are frequently observed.

A tentative model for the construction of FF nanotubes was proposed by Görbitz in 2006 (**Figure 1-23**). The exact nature of the inner surface shown in **Figure 1-23** is not known, it may be mixed hydrophobic/hydrophilic as shown, or entirely hydrophobic. The individual narrow channels proposed within the model are hydrophilic in nature and are able to accommodate guest molecules of some size as well as hydrated metal ions. The aromatic groups generate a striking three-dimensional aromatic stacking arrangement serving as a glue between the hydrogen-bonded cylinders of peptide main chains and promoting fibre formation. It was also proposed that the laminated construction provides exceptional strength for a low-density porous supramolecular network and makes this structure unique among organic materials.

In order to understand the compatibility of FF nanotubes with common lithographic techniques, as well as the long-term durability of nano-devices based on FF nanotubes, Adler-Abramovich and co-workers (2006) investigated the thermal and chemical instability of FF nanotubes. A cold field emission gun (CFEG) high-resolution scanning electron microscope (HRSEM) study showed that FF nanotubes dry-heated up to 150 °C were clearly stable with the same morphology as that observed for untreated FF nanotubes. A significant destruction

of the structures occurred when FF nanotubes were heated to 200-300 °C. They also reported that FF nanotubes were chemically stable in organic solvents such as ethanol, methanol, 2-propanol, acetone, and acetonitrile, as shown by SEM analysis. Using atomic force microscopy (AFM), Sedman and co-workers (2006) showed through in-situ heating studies that FF nanotubes kept its wall integrity at temperatures up to 100 °C. On increasing the temperature further to 150 °C, the nanotubes lost spatial volume. They argued that it was possible that the elevated temperature made the nanotubes more deformable and that they became distorted by the AFM probe during the imaging process. Time-of-flight secondary ion mass spectrometry (ToF-SIMS) analysis suggested that at temperatures at and above 150 °C, the loss in mass and apparent degradation in the nanotubes morphology was due to the loss of phenylalanine.

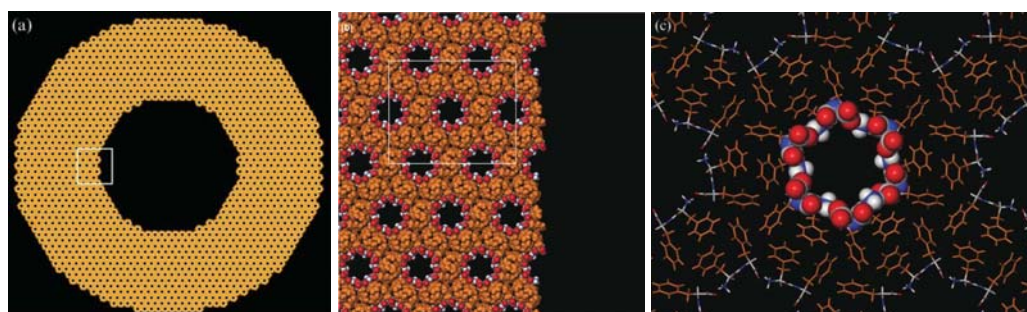


Figure 1-23 Model for the construction of hollow FF fibres. Atoms in the peptide main chains are colored according to atom type, while atoms in the phenylalanine side chains are depicted in orange. Shown in (a) is a tube with a 110 nm outer diameter and a 50 nm inner diameter. This is comparable to the average size obtained by Reches and Gazit (2003), but smaller than that obtained by Song (2004) and in the present investigation. The white square indicates the part enlarged in (b) showing a model of the peptide-channel interface at the inner surface. The rectangle represents the detailed view given in (c) in a capped sticks representation, but with atoms constituting the pore surface in spacefill (figure adapted from Gorbitz 2006).

The elasticity of FF nanotubes was investigated by Kol and co-workers (2005) using the AFM indentation method, and a Young's modulus of ~ 19 GPa was obtained. In chapter 6 and also in my recent publication (Niu *et al.* 2007), we built on these studies through application of the bending-beam model to AFM images of FF nanotubes suspended across cavities to obtain the Young's modulus and the shear modulus. We were able to utilize this method to study the influence of temperature and relative humidity on the elasticity of FF nanotubes.

Attempts to control the spatial organization of FF nanotubes have also been made. Reches and Gazit (2006) achieved vertical alignment of FF nanotubes by applying the FF peptide monomers dissolved in the organic solvent onto siliconized glass (**Figure 1-24** left). They also achieved horizontal alignment of FF nanotubes by assembling the FF peptide monomers in the presence of ferrofluid and then exposing formed nanotubes to an external magnetic field (**Figure 1-24** right). Hill and co-workers (2007) have also demonstrated that FF nanotubes align in a magnetic field without any additional treatment (**Figure 1-25**). They predicted that most of the magnetic torque on the structure to be generated by the diamagnetic anisotropy of the aromatic rings.

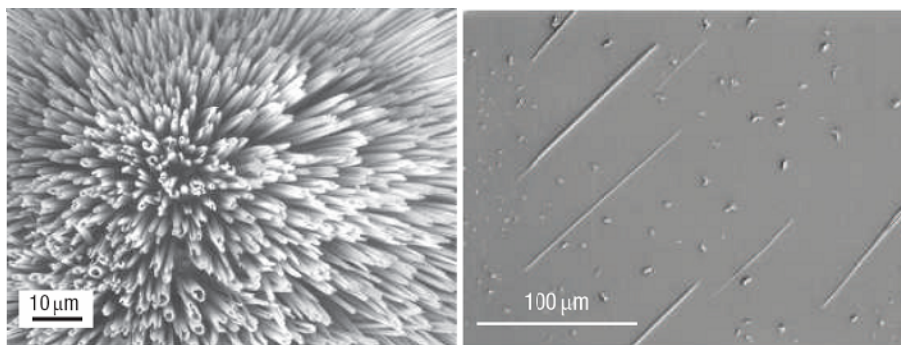


Figure 1-24 SEM images of controlled patterning of aligned diphenylalanine nanotubes. The left picture shows vertically aligned FF nanotubes. The FF peptide monomers were dissolved in the organic solvent and then applied onto siliconized glass. The right picture shows the horizontal arrangement of the aligned FF nanotubes. The FF peptide monomers self-assembled in the presence of ferrofluid and then were exposed to an external magnetic (figure adapted from Reches and Gazit, 2006).

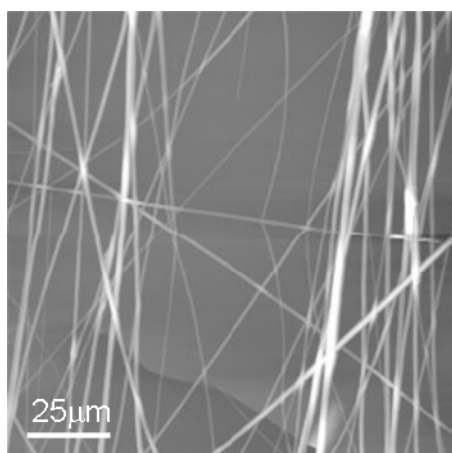


Figure 1-25 AFM topography images of aligned FF nanotubes. The droplet of HFIP–water solution containing FF nanotubes on mica was allowed to evaporate in applied magnetic fields of 12 T. The magnetic field direction lies in the plane of the substrate, along the direction from down to up (figure adapted from Hill *et al.* 2007).

1.3.3.3 Applications of Diphenylalanine Nanotubes

Reduction of ionic silver within FF nanotubes using citrate, followed by enzymatic degradation of the peptide backbone, resulted in the production of discrete silver nanowires with diameter $\sim 20\text{nm}$ (Figure 1-26) (Reches and Gazit 2003). The unique properties of FF nanotubes (see section 1.3.3.2) and their proteolytic lability allow their use as nanoscale molds for the casting of silver nanowires. Reches and Gazit claimed this study also proved that FF nanotubes are indeed hollow and filled with aqueous solution.

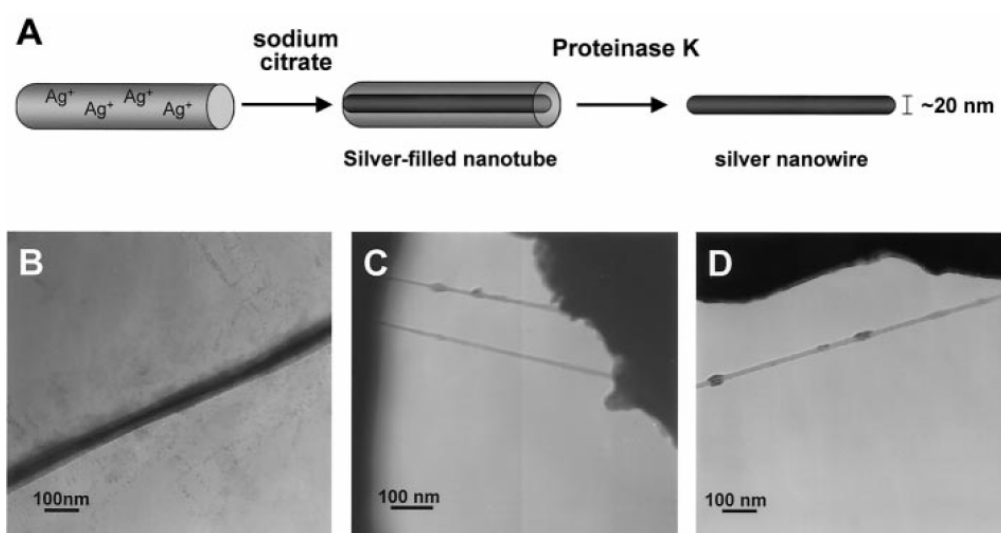


Figure 1-26 Casting of silver nanowires with the peptide nanotubes. (A) The nanowires were formed by the reduction of silver ions within the tubes, followed by enzymatic degradation of the peptide mold. (B) TEM analysis (without staining) of peptide tubes filled with silver nanowires. (C and D) TEM images of silver nanowires that were obtained after the addition of the proteinase K enzyme to the nanotube solution (figure adapted from Reches and Gazit 2003).

Song and co-workers (2004) reported the synthesis of platinum-nanoparticle peptide-nanostructure composites (**Figure 1-27**). Their work suggested that the walls of peptide nanostructures could be porous. The proposed porosity allowed the formation of novel nanocomposites without the disruption of the original nanostructure morphology. The composites prepared in their study has many potential applications, e.g., catalysis; they could also serve as useful scaffolds for the synthesis of other nanomaterials.

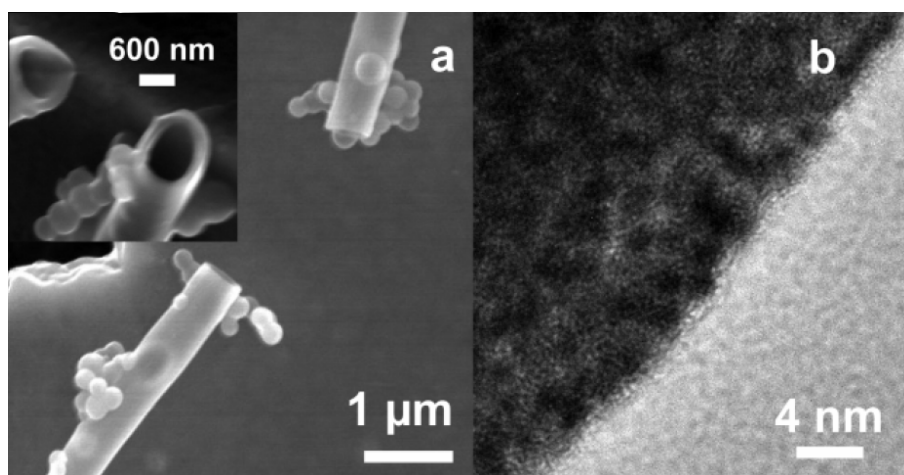


Figure 1-27 SEM images of (a) peptide nanotubes and nanovesicles containing Pt particles (inset: tilted image showing the tubes are hollow) and (b) a high resolution TEM image showing the 2 nm Pt nanoparticles embedded in the wall of a platinum nanotube (figure adapted from Song *et al.* 2004).

Using voltammetric and time-based amperometric techniques, FF nanotube modified graphite electrodes were demonstrated to have improved electrochemical reactivity for the potassium hexacyanoferrate oxidation-reduction reaction over non modified electrodes (Yemini 2004); the FF nanotubes modified gold electrodes, in addition, showed improved sensitivity for hydrogen peroxide

and NADH detection (Yemini 2005). These studies offered novel perspectives for the development of sensors and biosensors.

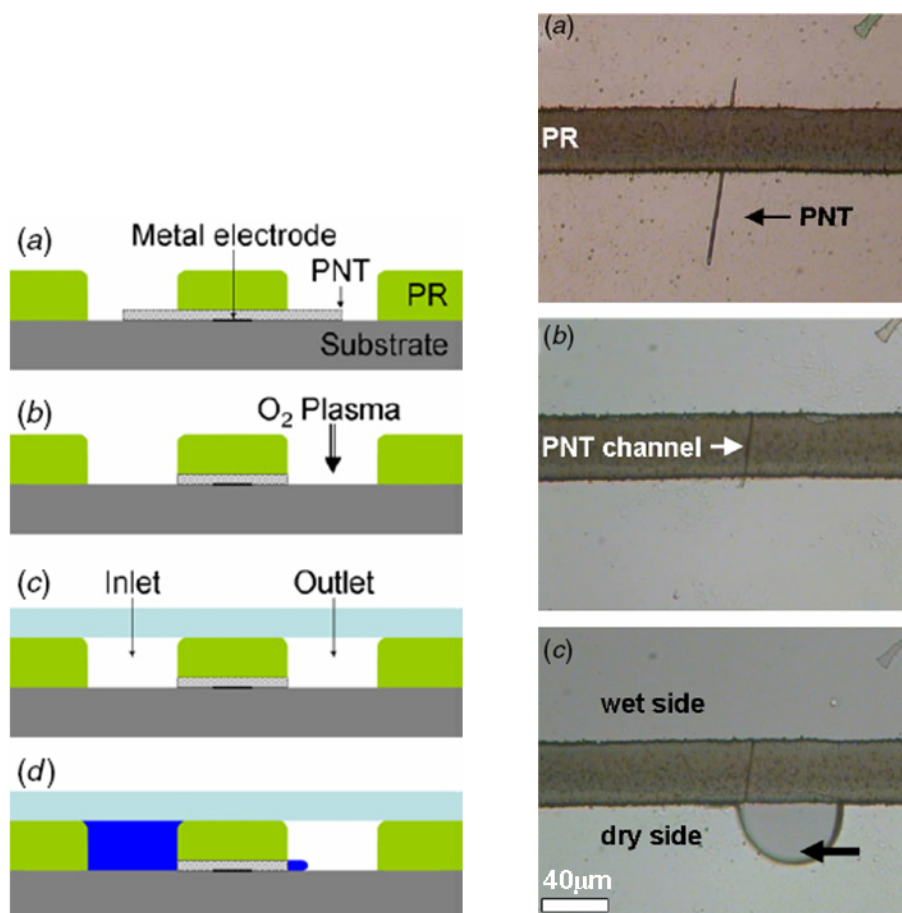


Figure 1-28 Integrating FF nanotubes in micro-fabrication processes. The left picture is a schematic shows the fabrication steps used to create protein nanotube (PNT) based fluidic channel. (a) Interfacing channels are formed using photoresist (PR); (b) unnecessary PNT parts are removed using O₂ plasma treatment and de-ionized water rinsing; (c) sealing the interfacing channel using a thin PDMS cap; (d) flow of solution via the PNT channel. The right picture is an optical image of a nano-fluidic channel using the steps described above. (a) A PNT based nano-fluidic channel before the final fabrication step of the PNT-end trimming; (b) a dry channel ready for use; (c) PBS flow through the nano-fluidic channel (figure adapted from Sopher *et al.* 2007).

Sopher and co-workers (2007) presented an adjusted photo-lithography compatible scheme that allowed the integration of FF nanotubes in micro-fabrication processes; specifically, a scheme for creating nano-fluidic channels using FF nanotubes (**Figure 1-28**).

Dipeptides linked to fluorenylmethoxycarbonyl (Fmoc-dipeptides) were found to entangle into fibrous hydrogels (Jayawarna *et al.* 2006; Mahler *et al.* 2006). These hydrogels were found to be stable under cell-culture conditions. Liebmann and co-workers (2007) utilized Fmoc-FF nanotube hydrogel for in situ 3D cell culturing. Their results showed that use of highly biocompatible Fmoc-FF hydrogel components significantly reduced the cytotoxic effects seen with alternate 3D culture materials. In addition, the peptide-derivative hydrogel simplified both handling and loading of the gel to the microstructures, with the ability to easily control the cell type, cell density and composition of each given hydrogel layer. They suggested that it was plausible to design and construct more complex culture systems, which opened the door to new possibilities and new approaches to cell biology. FF fibrils self-assembled in organic solvents can also entangle further to form gels (Yan *et al.* 2008). Yan and co-workers encapsulated quantum dots (QDs) into the FF gel and noted that this was an effective method to protect QDs from oxidation and improve the stability of QDs.

1.4 Aims and Outline of Research

As introduced above, protein nanotubes have a wide range of potential applications in biotechnology. The comprehensive understanding of the properties of these protein nanotubes has become a prerequisite of rational materials design.

The main purpose of the work presented in this thesis is to investigate how to obtain the structural and mechanical information of protein nanotubes utilizing the advantages of atomic force microscopy. Several different protein nanotubes introduced above will be used as examples to develop AFM methods.